

JPL PUBLICATION 78-17

Application of Digital Image Processing Techniques to Astronomical Imagery 1977

Jean J. Lorre
Donald J. Lynn

April 15, 1978

National Aeronautics and
Space Administration

Jet Propulsion Laboratory
California Institute of Technology
Pasadena, California

PREFACE

The work described in this report was performed by the Earth and Space Sciences Division of the Jet Propulsion Laboratory.

ACKNOWLEDGEMENTS

The activities described in this report were encouraged and supported by Dr. Charles O'Dell, Space Telescope Project Scientist at Marshall Space Flight Center, and Dr. Nancy Roman and Dr. Jeffrey Rosendahl at NASA Headquarters.

William B. Green, Manager of the Science Data Analysis Section that includes the JPL Image Processing Laboratory, was responsible for initiating the project.

I wish to thank Dr. Ivan King for his calibrated plates, Dr. René Racine for his photoelectric magnitudes of NGC6218, Dr. James Gunn and Dr. Thomas Kuiper for plates of Lick H α 101 and assistance in analysis and Dr. Halton Arp for his plates and suggestions.

CONTENTS

I.	Introduction	1
II.	Automated Object Location	2
III.	Polarization	3
IV.	Principal Component Transformation	5
V.	Color Enhancement	7
VI.	Faint Nebulosity Enhancement	9
VII.	Atmospheric Deconvolution	10
VIII.	Texture Images and Isophotes	12
IX.	Summary and Conclusions	13
X.	References	15

FIGURES

1.	Image of the globular cluster as presented to the object locator	16
2.	Each object found by the automated object locator (STARCAT) has been enclosed within a curve. An identifier has been placed beneath each object in order to associate it with a catalogue of computed magnitudes	17
3.	Photoelectric magnitudes are plotted versus magnitudes computed by the object finder. The mean error is about 0.1 magnitudes . . .	18
4.	Photoelectrically determined color index is plotted versus computed magnitude. A slight color dependent error is present due to differences between the V magnitude passband and the passband of the plate	19
5.	Intensity image obtained by averaging three polarization images each 60 degrees apart. The histograms correspond with the original images	20
6.	Intensity isophotes superimposed upon the intensity image	21
7.	Polarization picture. White corresponds to 12 percent polarization. The histograms are of the polarization, the polarization angle coded as brightness, and of the intensity	22

CONTENTS (Contd)

FIGURES (Contd)

8.	Polarization direction and magnitude are displayed as vectors. Isophotes are of the intensity image	23
9.	Polarization isophotes are displayed on the smoothed polarization picture. Each contour signifies a 2 percent change in polarization	24
10.	Polarization coded in a color display. Intensity is coded as brightness, polarization as degree of saturation, and vector orientation as hue	25
11.	The logarithm of the highest ranked Principal Component Transformation of four spectral bands. This image contains a weighted intensity average in which uncorrelated information and noise have been minimized	26
12.	The second ranked Principal Component Transformation of four spectral bands. This image contains the dominant color differences only in which no intensity information is present . . .	27
13.	The third ranked Principal Component Transformation of four spectral bands. This image contains less highly correlated color differences	28
14.	The fourth or lowest Principal Component Transformation of four spectral bands. This image contains that information which is uncorrelated between the four original bands. Most of the information visible is noise and plate mottling	29
15.	A color composite image produced by adding the three color coded lowest Principal Component Transformations	30
16.	The idealized coordinate system relating blue, green, and red cartesian coordinates with hue, saturation, and intensity polar coordinates	31
17.	Color reconstruction produced by combining blue = 103a0, green = IIIaJ, and red = 127-04 in a purely additive manner. Colors are discriminated only poorly by the eye	32
18.	Saturation enhanced color reconstruction. The same images used to produce Figure 17 were transformed to the HSI space and the saturation picture was contrast enhanced. Transforming back to blue, green, and red produces a color enhanced image where the colors are more readily recognized. The hues have not been altered	33

CONTENTS (Contd)

FIGURES (Contd)

19.	Saturation enhanced color reconstruction. The same images as Figure 18 were used except that before the inverse transformations was made to blue, green, and red, the intensity image was replaced by its logarithm. Discriminability is now nearly complete	34
20.	Color enhanced picture with blue = 103a0, green = IIIaJ, and red = 098. Both log intensity and contrast enhanced saturation have been performed	35
21.	Color enhanced picture with blue = 103a0, green = 127-04, and red = 098. Both log intensity and contrast enhanced saturation have been performed	36
22.	Color enhanced picture with blue = IIIaJ, green = 127-04, and red = 098. Both log intensity and color enhanced saturation have been performed	37
23.	Contrast enhanced picture of a single 127-04 plate. Plate mottling is sufficiently severe to mask much of the information in the image	38
24.	Background flattened image. This is the same plate as Figure 23 after processing with a one-dimensional Median filter. Faint structure in the plate background can be discerned now that much of the large scale mottling has been suppressed.	39
25.	The average of five IIIaJ plates has been processed to remove all of the larger stellar and galaxy images. Jets emanating from NGC1097 can be more readily observed	40
26.	The image in Figure 25 has been processed with a small Median filter to suppress small stellar images and plate grain	41
27.	Color reconstruciton using two stacks of flattened pictures. Blue = IIIaJ, and red = 127-04. Saturation enhancement was performed to reveal color differences in the jets	42
28.	The image in Figure 27 was modified by removing small stellar and grain structure with a small Median filter	43
29.	Deconvolution to compensate for atmospheric seeing. Top left is the original image and top right is the deconvolved image. The bottom row is the same as the top row with isophotes superimposed. A reference star has been inserted into the lower right corner of each quadrant	44

CONTENTS (Contd)

FIGURES (Contd)

30.	Deconvolution of the nuclear region of an elliptical galaxy in the same mosaic format as Figure 29	45
31.	Deconvolution of an elliptical galaxy nucleus	46
32.	Geometrically rectified mosaic of before deconvolution (left) and after deconvolution (right) to remove ellipticity caused by viewing geometry	47
33.	Mosaic of images of the central region of a globular cluster. Top left is the original blurred image. Top right is the deconvolved image. Bottom left is the blurred image after removal of the global object shape. Bottom right is the deconvolved image of the one to its left. Some resolution improvement is apparent	48
34.	Mosaic of the nucleus of M31. Each of the top four rows represent a separate plate. The left image is a reference star, the middle image is the blurred nucleus, and the right image is the deconvolved nucleus. The bottom row is the average of the top four rows	49
35.	Mosaic of the nucleus of M31 in the same format as Figure 34. A higher signal to noise ratio enabled more complete deconvolution than in Figure 34	50
36.	Isophote contours superimposed upon the mosaic of Figure 35	51
37.	Deconvolution of two plates of M87. The left side is the original, and the right side is deconvolved to separate the bright feature into two knots	52
38.	Intensity image of a galaxy showing a spiral pattern which is not symmetrically textured	53
39.	A picture illustrating the local standard deviation. The break in the ring around the galaxy indicates a difference in texture between the top and bottom halves	54
40.	Isophotes spaced at close intervals reveal the distribution of intensity in the vicinity of two line-of-sight galaxies	55

ABSTRACT

Nine specific techniques or combination of techniques developed by the Image Processing Laboratory of the Jet Propulsion Laboratory for applying digital image processing technology to existing astronomical imagery are described:

1. The development of automated object location, intensity, and cataloging algorithms.
2. The computation, generation and display of polarization information from image data.
3. The use of principal component transformations to segregate and display color structure and to compute optimally weighted intensity images.
4. The use of enhancement in the color domain to exaggerate and display small spectral differences.
5. The use of pseudo-color to identify and discriminate between regions having differing characteristics.
6. The use of non-linear spatial filtering techniques to extract and display only that structure lying within a desired size domain.
7. The deconvolution of atmosphere and instrument optical transfer functions from an image in order to achieve a moderate increase in resolution.
8. The use of texture maps and isophote contours to detect and display very subtle structural characteristics.
9. The use of multispectral classification techniques to combine and correlate observations taken at various wavelengths.

Photoproducts are included to illustrate the results of each of these investigations.

I. INTRODUCTION

This report describes work performed during 1977 at the Image Processing Laboratory (IPL) of the Jet Propulsion Laboratory under FY77 RTOP #188-41-58 and FY78 RTOP #389-41-01. The objective of this task was to investigate the applications of digital image processing technology to the analysis of astronomical imaging data, to acquaint members of the astronomical community with the possible scientific benefits of utilizing such technology, and to provide some insight into digital techniques that could be applied in ground processing of Space Telescope imagery.

With a few exceptions, the efforts described in this report have been performed using existing software at the Image Processing Laboratory that was originally developed for digital processing of NASA's planetary imagery (Green, 1975; Soha, 1975; Ruiz, 1977; Levinthal, 1977; Green, 1977) and remotely sensed Earth observations data from the Landsat satellites and other airborne multispectral sensors (Soha, 1976; Goetz, 1975). We feel that the activities described in this report represent a small number of the potential applications of digital image processing technology to astronomical investigations. Throughout this effort, new applications of computer image processing to astronomy became apparent, and the IPL is currently involved in follow-on activities in this area. The results presented in this report thus represent extensions of work reported previously (Arp, 1976; Lorre, 1975; Lorre, 1976) and provide an indication of the exciting new discoveries that will occur following the launch of NASA's Space Telescope in the early 1980's.

This report is divided into nine sections. Sections II through VIII each present a technique or combination of techniques developed or applied in performance of a specific analysis. The data used and the techniques involved are described. Photographic products are attached to illustrate the results. Section IX presents conclusions and observations which can be made as a result of this work.

This report deliberately avoids interpretation (however tempting) of physical results. This is because the data and the privilege of interpretation belongs to the astronomers with whom we collaborated. It is the purpose of this task only to show how digital image processing can aid the astronomer in his analysis and interpretation.

II. AUTOMATED OBJECT LOCATION

In order to be able to address many objects within a single image, a catalogue generating algorithm (STARCAT) was developed. This algorithm searches an image for contiguous pixels whose intensities (DN values) lie above a user-specified threshold. All contiguous pixels are integrated to give a total intensity and a centroid location for that intensity. These values are placed in a catalogue which can be accessed by other programs. It is possible in this manner to accumulate information on thousands of objects in a few minutes.

Figure 1 illustrates a scan of the central regions of NGC6218 on a plate supplied by Dr. Ivan King of the University of California, Berkeley. Figure 2 shows contours around each object located by the identifier STARCAT and a numerical designation used to catalogue each object for further study. In order to produce reliable integrated intensities, the plate background had to be eliminated. A special technique was used consisting of applying a Median filter (MEDIAN) of dimension greater than twice the largest real object in the image. The Median filter replaces each pixel by the median, or value half way up the histogram, of a neighborhood symmetrically to either side of (or around, depending upon dimensionality) the pixel. This filter has the advantage over linear filters in that objects less than half the filter width are not seen. Thus, an image of the background is produced which can be subtracted from the original image to produce a background-free (within the limits of the algorithm) image. An additional property of the filter is that any function which is monotonic within the filter width will be passed unchanged.

Photoelectric photometry of NGC6218 was obtained from Dr. René Racine of the University of Montreal, to compare with the integrated intensity determined by the program values. Figure 3 shows the results of plotting photoelectrically observed magnitude versus computed magnitude. The standard deviation of the error was 0.1 magnitude which we feel is good considering that the data was digitized only to 7 bits (128 levels). In Figure 4, the error in magnitude is plotted versus the photoelectric color index. One can see a slight magnitude shift of about .1 magnitude in the error, due most likely to discrepancies between the passband of the 103aD + GG11 plate/filter and "V" in the photoelectric system.

Automatic techniques such as these could be used to process large images containing millions of objects. Data acquired digitally (avoiding the photographic process) should allow one to process a much greater range of magnitudes and give more accurate results.

III. POLARIZATION

A set of three IIIaJ plates of the early type object Lick H α 101 were obtained from Dr. James Gunn of Caltech. These plates were taken through polarizers oriented at 0°, 60°, and 120° respectively. Dr. Thomas Kuiper of JPL was involved in the derivation of the polarization equations and in interpretation of the results.

Given three images taken through polaroids of orientation 0°, 60°, and 120° measured clockwise from the vertical (each picture element has intensity component I_1 , I_2 , and I_3), the following equations describe the polarization P and orientation ϕ for each pixel.

$$K = \frac{2}{3} (I_1 + I_2 + I_3)$$

$$I_p^2 = 4I_1^2 - 4I_1K + K^2 + \frac{4}{3} (I_2 - I_3)^2$$

$$P = I_p/K$$

$$S = \frac{4}{3} (I_2 - I_3)$$

$$C = 2I_1 - K$$

$$2\phi = \text{Tan}^{-1} (S/C)$$

The three images were registered by correlating individual stars in two of the images to their counterparts in the third image. Before any evaluation was performed, the three images were detrended by subtracting a plane fitted through background points around the periphery of the scanned image. This step was necessary to minimize the mottling characteristic of IIIaJ emulsions. The images were linearly modified in intensity so that each image had the same mean DN value and the same standard deviation. Unfortunately, it seems difficult to avoid some pre-processing of this sort when both low spatial frequencies and film are involved.

The Program POLARIZE was developed to determine the amount of polarization and its orientation by evaluating the above equations at each point in the image. In order to improve the apparent signal-to-noise, the intensity at each pixel was replaced by the average intensity of a 5x5 pixel area centered on that point for each of the three images. This step minimizes the high frequency noise to the point where consistent results were obtainable. Figure 5 shows the intensity image (K) obtained by averaging the three inputs. An isophote map of the intensity is shown in Figure 6.

The resulting polarization and vector orientation maps are shown in Figures 7 and 8. The histograms below the intensity image give the distribution of intensity for each of the three input images as well as for the average. Similarly, histograms below the polarization image represent (from upper left) the Degree of Polarization, the Polarization Angle coded as brightness, the Average Intensity, and the contrast enhanced Polarization Histogram for the subject image. In Figure 7, white represents a polarization value of about 10% and black is 0.0.

Because the polarization is so small, there is little signal-to-noise left in the data and one must interpret very small structure with caution. In Figure 9, contours representing 2% increments in polarization have been placed on the smoothed polarization image.

A color image was created (Figure 10) by coding the intensity as brightness, the polarization as saturation, (i.e., purity of color, pastel shades being low polarization values), and vector orientation as hue (i.e., the mean wavelength of the color). This scheme lends itself to a polar coordinate diagram which will be discussed later in the color enhancement section. Stellar images appear colored because of small registration errors. The bright red spot towards the image center is a blemish on one of the plates.

This color representation contains the intensity, polarization, and vector orientation all in one image. With a little practice, a person can become quite adept at determining vector orientations from hues. We feel this is a useful and compact way of representing polarization both quantitatively and qualitatively.

IV. PRINCIPAL COMPONENT TRANSFORMATION

Images obtained in four spectral bands were made available by Dr. Halton Arp, of Hale Observatories, for the galaxy NGC1097. These images were converted into intensity units using calibration spots provided on the plates. The bands were Green = IIIaJ + GG385, Red = 127-04 + RG610, UV = 103a0 + UG5, and H α interference. There was, however, no calibrated relationship between the bands themselves. Of the four bands, the Green image was the average of five digitally registered IIIaJ plates, and the Red image was the average of two 127-04 plates.

The Principal Component Transformation (Ready and Wintz, 1973) performs a rotation and translation of the N dimensional (in this case, four dimensional) histogram space such that the covariance matrix of the images is diagonalized. The covariance matrix K of images of intensity I is defined by:

$$K_{ij} = \frac{1}{(\ell_2 - \ell_1 + 1)(s_2 - s_1 + 1)} \sum_{\ell=\ell_1}^{\ell_2} \sum_{s=s_1}^{s_2} (I_{i,\ell,s} - \mu_i)(I_{j,\ell,s} - \mu_j)$$

where i and j denote spectral bands, μ_i and μ_j are the mean intensities of each band, and ℓ_1, ℓ_2, s_1, s_2 denote the range of line and sample over which K is to be evaluated. In order to compute the required diagonalizing transformation, the eigenvalues or solutions to the characteristic polynomial must be computed:

$$\begin{pmatrix} K_{11} - \lambda & K_{12} & \dots & K_{1n} \\ K_{21} & K_{22} - \lambda & \dots & K_{2n} \\ \vdots & \vdots & \ddots & \vdots \\ K_{n1} & K_{n2} & \dots & K_{nn} - \lambda \end{pmatrix} = 0$$

The Principal Component Transformation is the matrix R in the following expression with column vectors normalized to unit length.

$$R^t K R = K^1$$

where t denotes transpose, and K^1 is the matrix having the eigenvalues solved for above.

When the output images of the Principal Component Transformation, as computed by the program EIGEN, are ranked in order of eigenvalue, they also represent the rank of signal-to-noise content. The first transformed image represents a sum of weighted intensity of the four original images. Subsequent transformed images con-

sist of linearly weighted differences of the original images. The last image contains information which has little correlation; this includes primarily random noise and plate inhomogeneities.

The Principal Component Transformation can be intuitively understood from the N-dimensional histogram. Because the input images were highly correlated in intensity, the histogram is dominated by a condensation of information along the main diagonal or achromatic (gray) axis. The transformation rotates and translates the histogram such that the orthogonal coordinate axes lie co-linear with the thickest sections through the histogram space. The first output image then, for example, corresponds with that axis which coincides with the main condensation described above.

Figures 11 through 14 display the four PCT images consisting of linear combinations of the four original images. The first is purely intensity (in this case log intensity) and the last contains mostly noise and plate mottling. Figures 12 and 13 display the spatial color distribution of the galaxy. HII regions are much easier to see now. Figure 15 shows a color composite made from the last three transformed images. Colors here are arbitrary codings of true color differences. Rings around the nucleus of NGC1097 are not real. They are due to incorrect relative intensity relationships between the original four images. The color composite of Figure 15 presents the most compact representation possible in single images of this color structure.

V. COLOR ENHANCEMENT

The same images in four bands of NGC1097 were used to create images with greatly exaggerated color. With this process only three images can be processed at one time, requiring four combinations to exhaust the information content of the original four bands. If one is given three images to be coded as Blue, Green and Red (BGR), one can convert them into three images corresponding to the physiological parameters representing Hue, Saturation and Intensity (HSI) (Gillespie, 1975). Figure 16 illustrates the relationship between BGR and HSI.

The BGR coordinates are first converted into x,y and z coordinates with the following two rotations.

$$\begin{bmatrix} x \\ y \\ z \end{bmatrix} = \begin{bmatrix} \frac{1}{\sqrt{3}} & \frac{\sqrt{2}}{\sqrt{3}} & 0 \\ -\frac{\sqrt{2}}{\sqrt{3}} & \frac{1}{\sqrt{3}} & 0 \\ 0 & 0 & 1 \end{bmatrix} \begin{bmatrix} \frac{1}{\sqrt{2}} & 0 & \frac{1}{\sqrt{2}} \\ 0 & 1 & 0 \\ -\frac{1}{\sqrt{2}} & 0 & \frac{1}{\sqrt{2}} \end{bmatrix} \begin{bmatrix} B \\ G \\ R \end{bmatrix}$$

H,S, and I images can then be created from the following definitions based upon Figure 16.

$$H = \text{Tan}^{-1} \left[\frac{\sqrt{z}}{-\sqrt{x}} \right]$$

$$S = \text{Cos}^{-1} \left[\frac{\sqrt{y}}{\sqrt{x+y+z}} \right] / \phi_m(H)$$

$$I = (x+y+z)/I_m(H,\phi)$$

where $\phi_m(H)$ is the maximum colatitude permitted for any hue, and $I_m(H,\phi)$ is the maximum intensity permitted at any given hue and colatitude. ϕ_m and I_m are necessary to avoid negative intensities in any of the BGR coordinates. When three images (B,G,R) have been transformed into H,S,I images using the HSI transformation, they can be manipulated individually. Figure 17 shows a color reconstruction made of images of NGC1097 taken in the bands 103a0, IIIaJ and 127-04 by additively recombining them. Colors can be seen only with difficulty because differences in color are small compared to intensities. However, when one enhances (with a single linear function) the contrast in the saturation image and then retransforms back to a new B,G,R, triplet, the additive reconstruction (Figure 18) effectively reveals

ORIGINAL PAGE IS
OF POOR QUALITY

color differences. One can further enhance the displayed information content by boosting lower intensities in the intensity image I with a logarithmic transfer function before retransforming back to B,G, and R. When one combines both processes (contrast enhancement in saturation and in intensity) the result is that of Figure 19. At no time have the hues been altered from those intrinsic in Figure 17.

In many cases such as the one here, one doesn't know the true relative intensities among the three bands. In this case, one can manipulate the three bands in such a way as to reveal the most color information possible even if the hues themselves are false in an absolute sense. After linearizing the digital pixel values, one can linearly modify two of the images so that the mean value and standard deviation are the same for all three input bands. This assures that the information content (variance) of each image is the same (they all contribute an equal amount of color) and further assures (and this is most important) that relative color differences are revealed in such a way that they can be discerned visually. The HSI transformation can then be applied. In certain applications, relative color is more useful than true enhanced color. For example, if one of the bands was twice as bright as the other two and if this were deliberately arranged to conform to some true, physical calibration, then the enhanced color would all be the same and the color product would be no more valuable than a gray level image in spite of the fact that the resulting color was "true".

Figures 20 through 22 display triplet combinations of the four input bands of NGC1097. The combinations are listed in Table 1.

TABLE 1

FIGURE	BLUE	GREEN	RED
19	103a0	IIIaJ	127-04
20	103a0	IIIaJ	098 (H α)
21	103a0	127-04	098 (H α)
22	IIIaJ	127-04	098 (H α)

These images reveal a wealth of population, chemical composition, and excitation distribution in the galaxy.

It is apparent that "true" color has not been preserved in these last four figures because of the mixing and reassignments of broad and narrow bands. The value of Figures 19-22 lies in the use of color to discriminate between regions with different spectral properties.

VI. FAINT NEBULOSITY ENHANCEMENT

Seven broadband images of NGC1097 were used to search for faint nebulosity in that galaxy. These images consisted of five 3aJ and two 127-04 plates obtained from Dr. Halton Arp of Hale Observatories. A one dimensional Median filter (as described in Section II) was applied to each image; the size was chosen to pass all real structure. The resulting low-noise image was smoothed with low pass filters and was then subtracted from the original image to yield an image in which large scale plate shading due to emulsion variations had been eliminated. A typical original image is shown in Figure 23; a shading removed image is shown in Figure 24.

After shading removal, the intensities and contrast were adjusted by making the mean intensity and variance of each image equal. All the images in each band were then averaged. The object locating program STARCAT described in Section II was then applied to the average image and a catalogue was created of the positions and sizes of every star and galaxy in the image. A program called STAREM2 was then run which, with the aid of the catalogue, removed every identified object from the image and replaced it with a plane fitted to the surrounding pixels. Random noise was added to each obliterated region to mask the process. Figure 25 shows the result when this process was applied to the average of the five 3aJ images.

Finally, a small Median filter followed by a small low-pass filter was run on each image to suppress tiny faint stars and random noise. The resulting image is shown in Figure 26. One can clearly see the three known jets. In addition, there appears to be a linear feature extending from the center of the galaxy toward the bottom right corner of the image. This feature has not been previously reported.

The color enhancement process discussed in Section V was applied to the averaged IIIaJ and 127-04 stacks. A third color image was generated by averaging the IIIaJ and 127-04 images. Color assignments were IIIaJ=Blue, IIIaJ and 127-04 averaged=Green, and 127-04=Red. Figures 27 and 28 show enhanced color both before and after removal of small structure. It can be seen that the downward extending jet is redder than the other jets.

VII. ATMOSPHERIC DECONVOLUTION

A number of carefully calibrated plates were obtained from Dr. Ivan King. Each image contained either the nucleus of a galaxy or some stellar type object and several reference stars. After linearizing the images using intensity calibration spots provided on the plates, the images were deconvolved using the reference stars to determine appropriate Point Spread Functions. In each case, a noise additive, frequency independent Wiener model was used in the deconvolution (Arp, 1976):

$$\text{ROTF}(f_x, f_y) = \text{OTF}^*(f_x, f_y) / (|\text{OTF}(f_x, f_y)|^2 + \text{SN}^{-2})$$

where ROTF is the Reciprocal Optical Transfer Function; f_x, f_y are orthogonal spatial frequencies in cycles/sample; and OTF is the Optical Transfer Function (the Fourier Transform of the Point Spread Function). SN is a constant signal-to-noise term used in lieu of the classical power spectrum ratio. In each case, the value of SN was varied until a visually optimal result was obtained. The Fourier Transform (FT) of the degraded image (I') was multiplied by the ROTF to obtain the FT of the partially restored image (I):

$$\text{FT}_{f_x f_y}(I) = \text{FT}_{f_x f_y}(I') \cdot \text{ROTF}(f_x, f_y)$$

Restored versions of the image were obtained by performing the inverse FT on $\text{FT}(I)$. No symmetric approximations were made because of the often clearly asymmetrical (complex nature of the OTF) properties of the Point Spread Function.

Numerous objects were processed with the above procedure using the program RESTORE. Figure 29 illustrates this process as performed on an image of the IR source NML Cygnus. The left side is the original image and the right is the partially deconvolved image. The bottom row is an isophote contoured version of the top row. For reference, a nearby star was moved next to NML Cygnus (in the lower right corner of each of the four squares) so that one could better judge the relative sizes of the images. This picture was processed with an SN value of 9.0, giving a maximum signal boost of 9/2 at some intermediate spatial frequency.

Figures 30 and 31 show similar processing on NGC4472 (M4a) and NGC4621 (both galactic nuclei) with SN values of 3 and 6 respectively. Figure 32 shows NGC4621 geometrically transformed in order to remove the viewing aspect ratio. Subsequent transformation of this image into polar coordinates centered about each

nuclei produced mean radial profiles. Figure 33 is a mosaic of four versions of the nuclei of the globular NGC7078. The upper left shows the original intensity image. To the right of it is the standard deconvolved image. The lower left image is the same as the blurred one above it except that the overall luminosity distribution of the object has been detrended in order to reduce the intensity range. The lower right is the deconvolved, detrended image. Detail in the nucleus is more readily apparent after both the detrending and deconvolution operations.

Four coude images each of the nucleus of M31 and M32 were also deconvolved using nearby stars in order to place upper limits on the sizes of these sources. Figures 34 and 35 show the results, the former being M31 and the latter being M32. Each of the top four rows represent the image from one plate. From left to right in each row, is the blurred reference star, the blurred object, and the deconvolved object.

The bottom row is the average of the top four rows. Averaging allowed a higher than normal SN value to be used to deconvolve each image. The sizes of the nuclei are noticeably smaller in both objects. Figure 36 shows contours superimposed upon the M32 mosaic (Figure 35). In Figure 36, the combined benefits of averaging and deconvolution are readily apparent over the use of either method alone.

An example of similar deconvolution of the jet in M87 is presented in Figure 37. The two images on the left are from plates taken by Dr. Arp. At the right, are deconvolved versions of the corresponding ones to the immediate left. The lower plate was obtained with better seeing and may reveal a slightly linear nature to one of the outer condensations. The condensations clearly have separate centers.

It is important to recognize that deconvolution will produce some artifact in the restored image. An explanatory note is in order.

Signal-to-noise is usually the limiting factor in any deconvolution attempt. The Wiener model optimizes in the presence of noise by producing an image which differs less in a global least squares sense from the true object than does the degraded image. Thus, the restored image is not guaranteed to resemble, at every point, what we are accustomed to observing and often contains artifacts caused by incomplete restoration.

VIII. TEXTURE IMAGES AND ISOPHOTES

A plate of NGC4380 taken by Dr. Arp was processed in order to enhance global structural asymmetries. Figure 38 shows a highly contrast-enhanced intensity image of the galaxy. It is apparent that the nature of the tight spiral structure differs in texture between the top and bottom of the image. In order to reveal textural distribution, objects near the bottom of the galaxy were removed and a standard deviation picture was produced (using the program PIXSTAT2) using a region which subtended many spiral bands. This image is shown in Figure 39. The uniform band of activity enclosing the galaxy disappears towards the bottom of the galaxy indicating a change in structure with possible interaction with another object.

The possible existence of faint absorption bands lying between overlapping galaxies can be investigated with isophotes. In Figure 40, an image taken from a photographically stacked series of plates obtained by Dr. Arp was isophote-contoured to reveal the distribution of luminosity between NGC1199 and a line-of-sight neighbor. Atypical inward bends of the isophotes toward NGC1199 in the vicinity of the apparent neighboring galaxy would be evidence of the presence of an absorption ring.

ORIGINAL PAGE IS
OF POOR QUALITY

IX. SUMMARY AND CONCLUSIONS

Seven different applications of digital image processing techniques to data obtained from scanned photographic plates have been presented. Some observations regarding the use of these techniques in astronomical research can be made:

1. It is possible and practical to automatically recognize, locate, and catalogue objects contained in an astronomical image and to be able to compute the corresponding intensities with reasonable accuracy.
2. Relatively straightforward image processing techniques can be used to compute and display polarization information in an image format. The use of color permits object brightness and polarization vector magnitudes and directions to be displayed in a single image, thus permitting areas of common and differing polarization characteristics to be readily identified.
3. Principal Component Transformations can be effectively utilized to automatically segregate and display color structure and to compute optimally weighted intensity images.
4. Color enhancement can be used to exaggerate and display small spectral differences in the same way that contrast enhancement is used to exaggerate and display small intensity differences. By transforming into other representations, such as HSI (Hue, Saturation and Intensity) space, small differences in color can be revealed without altering the effective wavelength at each point.
5. Even if it is not possible or desirable to display true color information, pseudo-color can be very effectively used to discriminate between regions having differing characteristics.
6. Non-linear spatial filtering techniques can be used to display only that structure in an image which lies within a desired object size. Thus, such visual distractions as variations in the plate background and high frequency content can be removed from an image in order to permit more desirable subtle information to be displayed and detected.
7. Optical transfer functions introduced by the atmosphere and instrument can be deconvolved from an image (if they can be adequately modeled or approximated) in order to obtain a moderate increase in resolution.

8. Isophote contours and texture maps can be utilized to detect and display spatial characteristics and variations which are too subtle to be seen in a normal display.
9. Multispectral classification techniques can be utilized to combine and correlate observations taken over the entire electromagnetic spectrum.
10. This work barely scratches the surface of applications of digital image processing to astronomical imaging. As new techniques were developed or applied during this effort, additional applications and techniques became apparent. For instance, none of the work described herein was concerned with spectra, yet some of these same techniques could be utilized to correlate, analyze and display information from spectra.

It is hoped that the techniques and results presented in this report will spur the imagination and curiosity of other astronomers who are looking for new ways of extracting and displaying information from their data. We invite those readers of this report who would like to pursue the application of these and other techniques to their particular problems, or to discuss possible applications, to contact the authors.

X. REFERENCES

1. Green, W.B., P.L. Jepsen, J.E. Kreznar, R.M. Ruiz, A.A. Schwartz and J.B. Seidman, "Removal of Instrument Signature from Mariner 9 Television Images of Mars," *Appl. Opt.* 14 (105) 1975.
2. Soha, J.M., D.J. Lynn, J.J. Lorre, J.A. Mosher, N.N. Thayer, D.A. Elliott, W.D. Benton and R.E. Dewar, "IPL Processing of the Mariner 10 Images of Mercury," *J. Geophys. Res.* 80 (17), June, 1975.
3. Ruiz, R.M., D.A. Elliott, G.M. Yagi, R.B. Pomphrey, M.A. Power, K.W. Power, K.W. Farrell, J.J. Lorre, W.D. Benton, R.E. Dewar and L.E. Cullen, "IPL Processing of Viking Orbiter Images," *J. Geophys. Res.* 82 (September 5, 1977).
4. Levinthal, E., W.B. Green, K.L. Jones and R.B. Tucker, "Processing the Viking Lander Camera Data," *J. Geophys. Res.* 82, (September 5, 1977).
5. Green, W.B., "Computer Image Processing - The Viking Experience," *IEEE Transactions on Consumer Electronics*, Vol. CE-23, No. 3 (p. 281), 1977.
6. Soha, J.M., A.R. Gillespie, M.J. Abrams and D.P. Madura, "Computer Techniques for Geological Applications," *Proceedings of the Caltech/JPL Conference on Image Processing Technology, Data Sources and Software for Commercial and Scientific Applications*, JPL SP-43-30, Jet Propulsion Laboratory, Pasadena, Calif., November, 1976.
7. Goetz, A.F.H., et.al., "Application of ERTS Images and Image Processing to Regional Geologic Problems and Geologic Mapping in Northern Arizona," *JPL Technical Report 32-1597*, Jet Propulsion Laboratory, Pasadena, Calif., May, 1975.
8. Arp, H., Lorre, J.J., *Image Processing of Galaxy Photographs*, *Ap.J.*, 210, p. 58, 1976.
9. Lorre, J.J., *Analysis of the Nebulosities near T-Tauri Using Digital Computer Image Processing.*, *Ap.J.*, 202, p. 696, 1975.
10. Lorre, J.J., Lynn, D.J., Benton, W.D., *Recent Developments at JPL in the Application of Digital Image Processing Techniques to Astronomical Images*, *SPIE Proceedings*, Vol. 74, P. 234, 1976.
11. Ready, P., Wintz, P., *Information Extraction, SNR Improvement, and Data Compression in Multispectral Imagery*, *IEEE Transactions on Communications*, Vol. Com-21, No. 10, October, P. 1123, 1973.
12. Gillespie, A., *Digital Processing of ERTS Images*, *JPL Technical Report 32-1597*, P. 168, Jet Propulsion Laboratory, Pasadena, Calif., 1975.



Fig. 1. Image of the globular cluster as presented to the object locator (NGC6218)

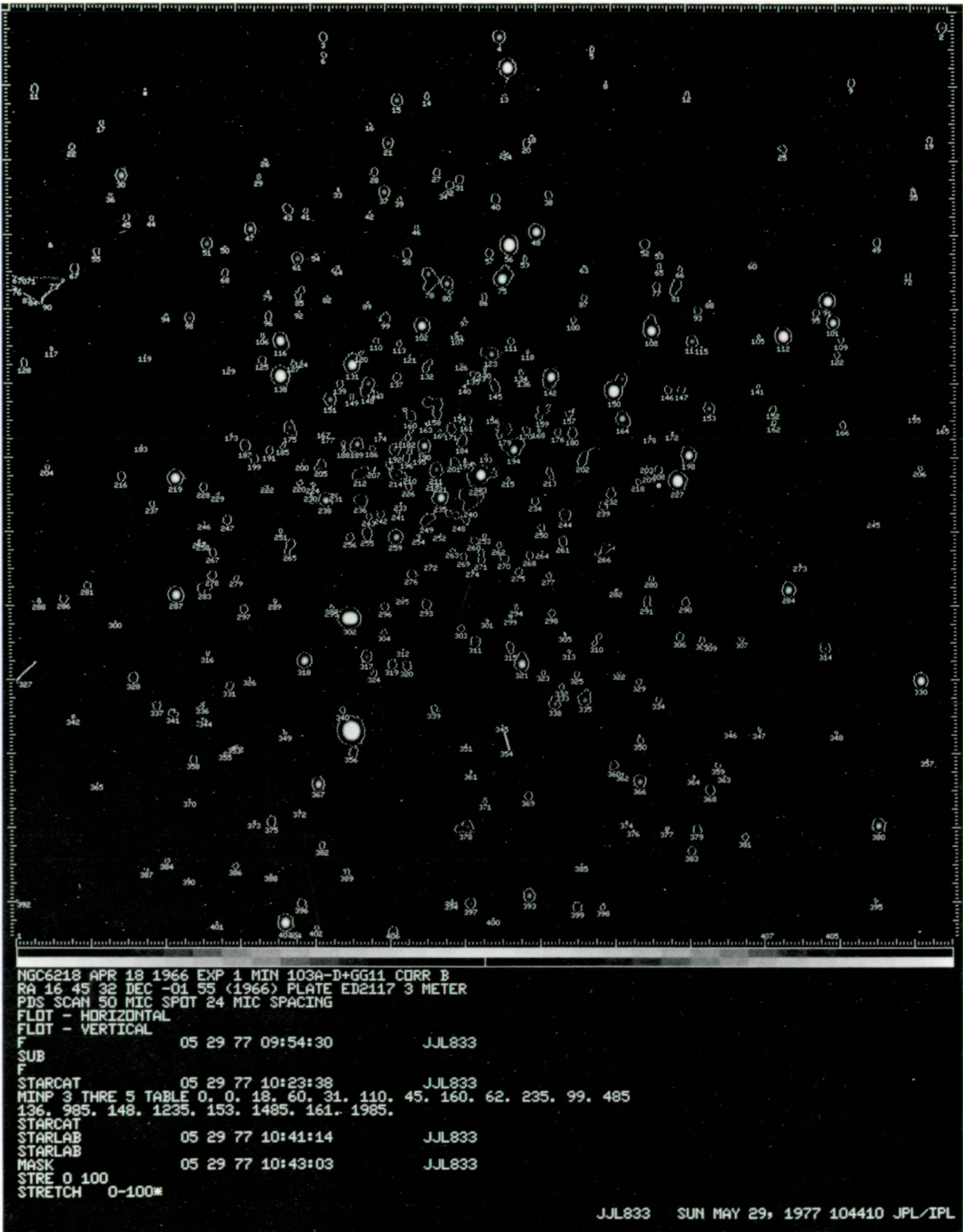


Fig. 2. Each object found by the automated object locator (STARCAT) has been enclosed within a curve. An identifier has been placed beneath each object in order to associate it with a catalogue of computed magnitudes (NGC6218)

ORIGINAL PAGE IS
OF POOR QUALITY

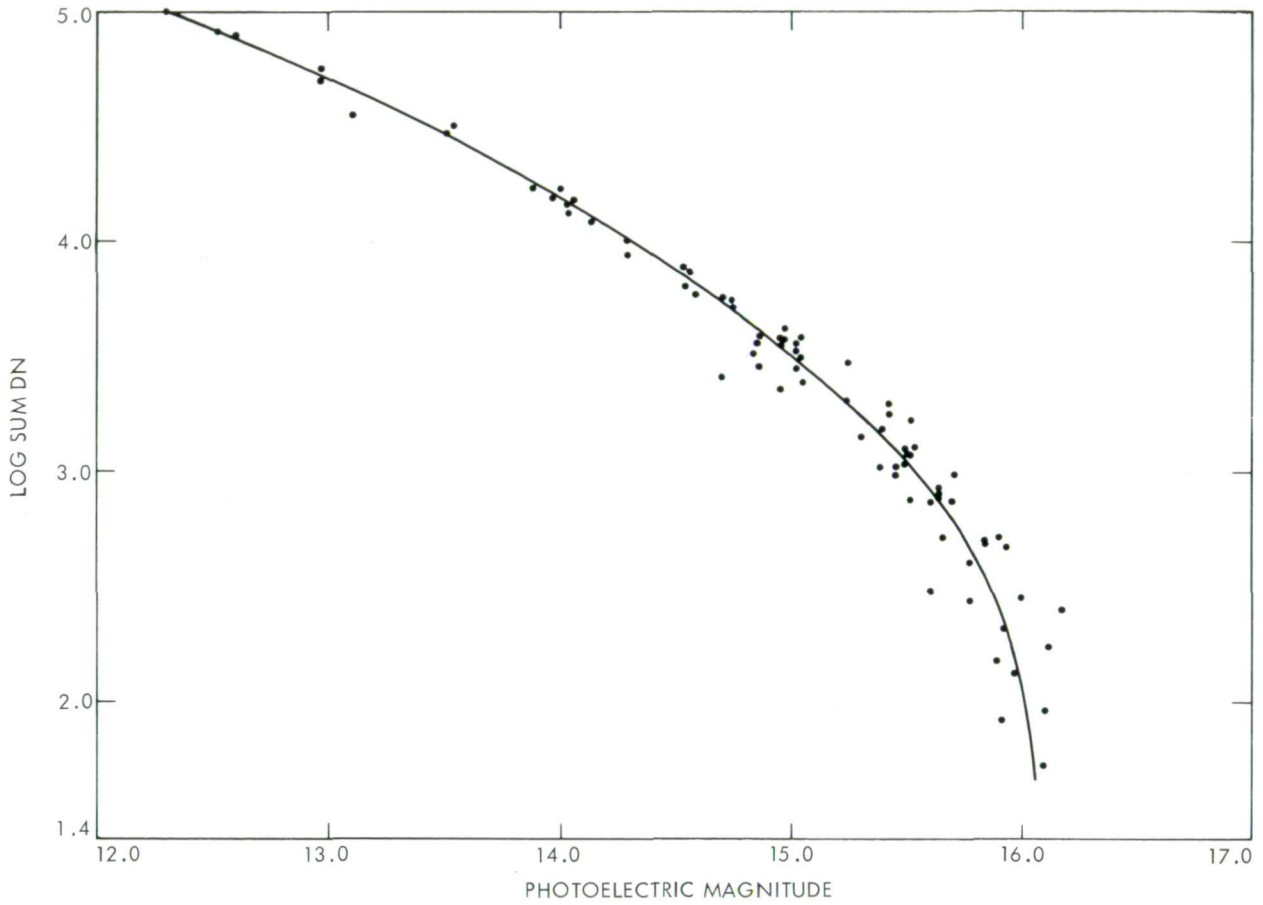


Fig. 3. Photoelectric magnitudes are plotted versus magnitudes computed by the object finder. The mean error is about 0.1 magnitudes (NGC6218)

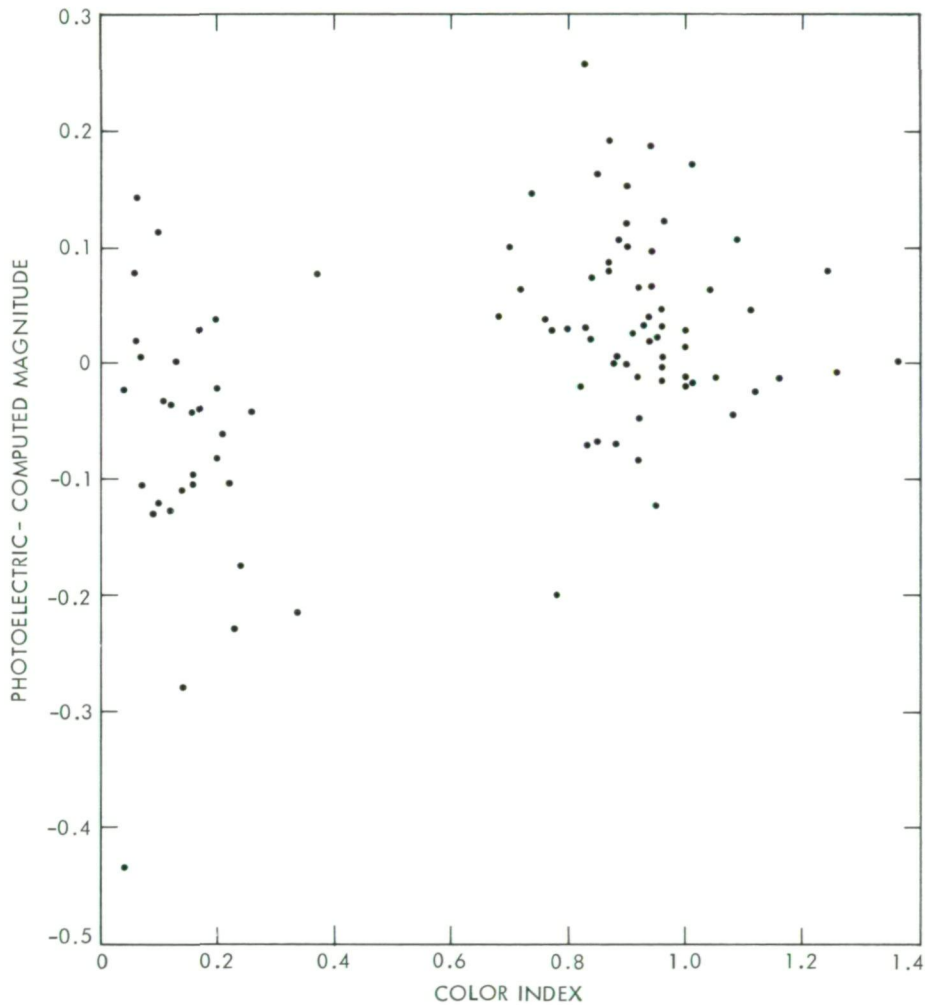


Fig. 4. Photoelectrically determined color index is plotted versus computed magnitude. A slight color dependent error is present due to differences between the V magnitude passband and the passband of the plate (NGC6218)

ORIGINAL PAGE IS
OF POOR QUALITY

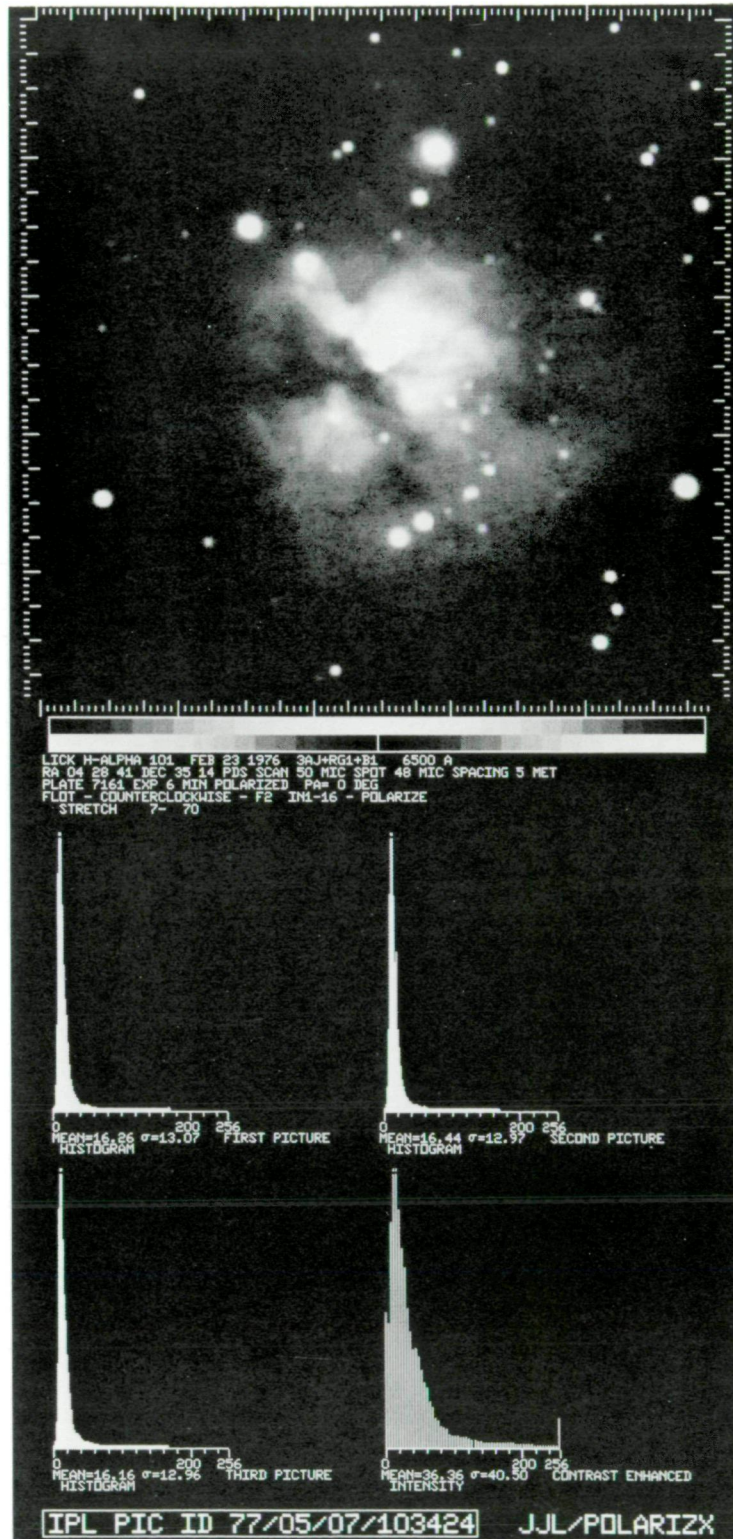
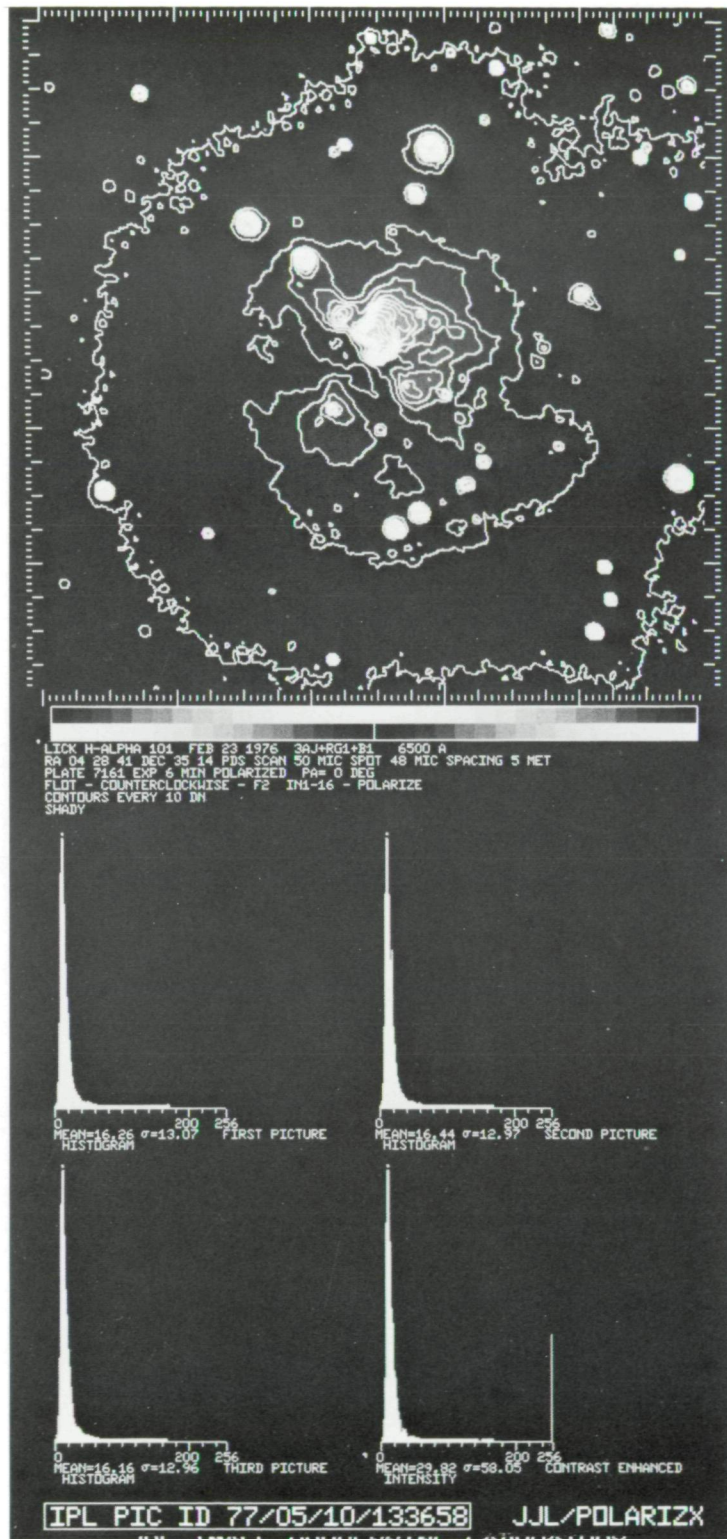


Fig. 5. Intensity image obtained by averaging three polarization images each 60 degrees apart. The histograms correspond with the original images (LICK H α -101)



ORIGINAL PAGE IS
 OF POOR QUALITY

Fig. 6. Intensity isophotes superimposed upon the intensity image (LICK H α -101)

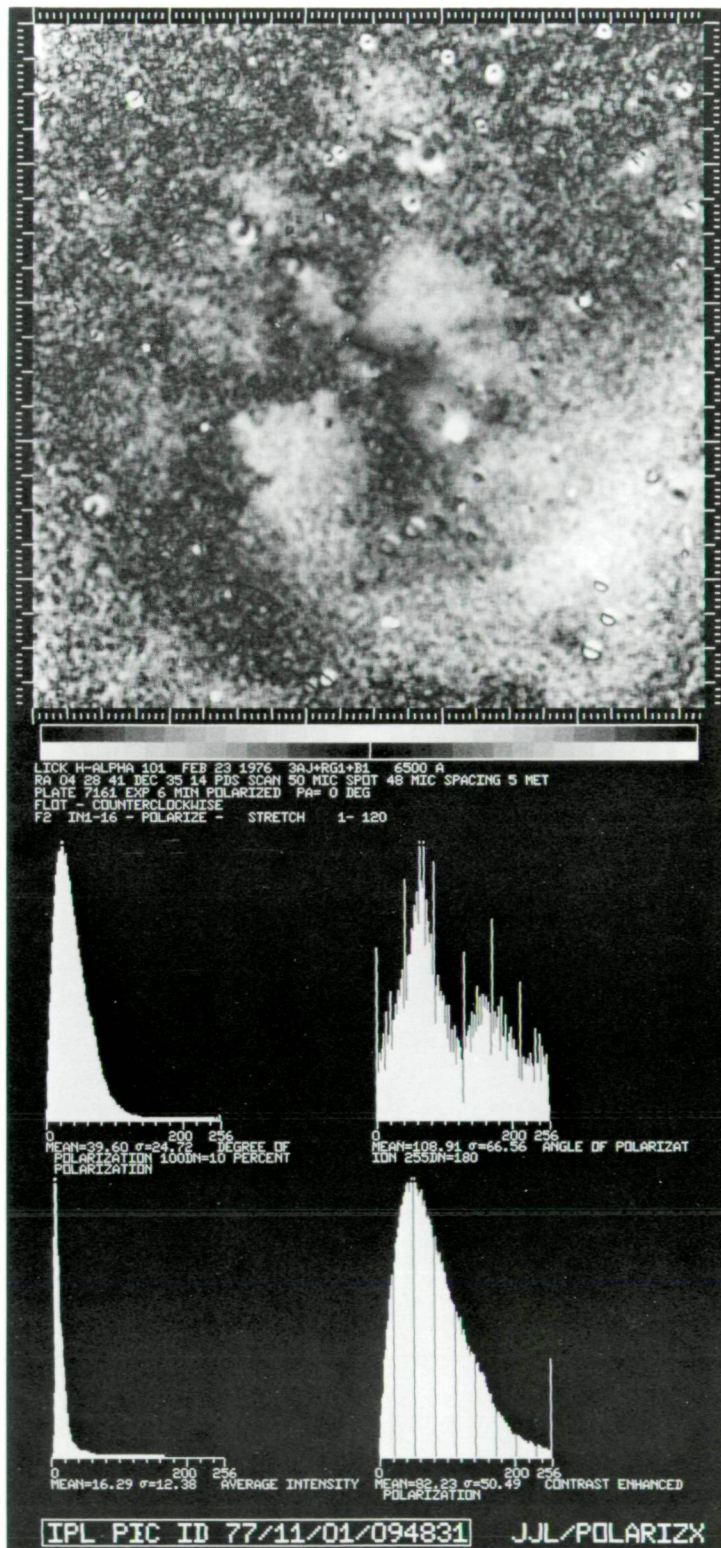
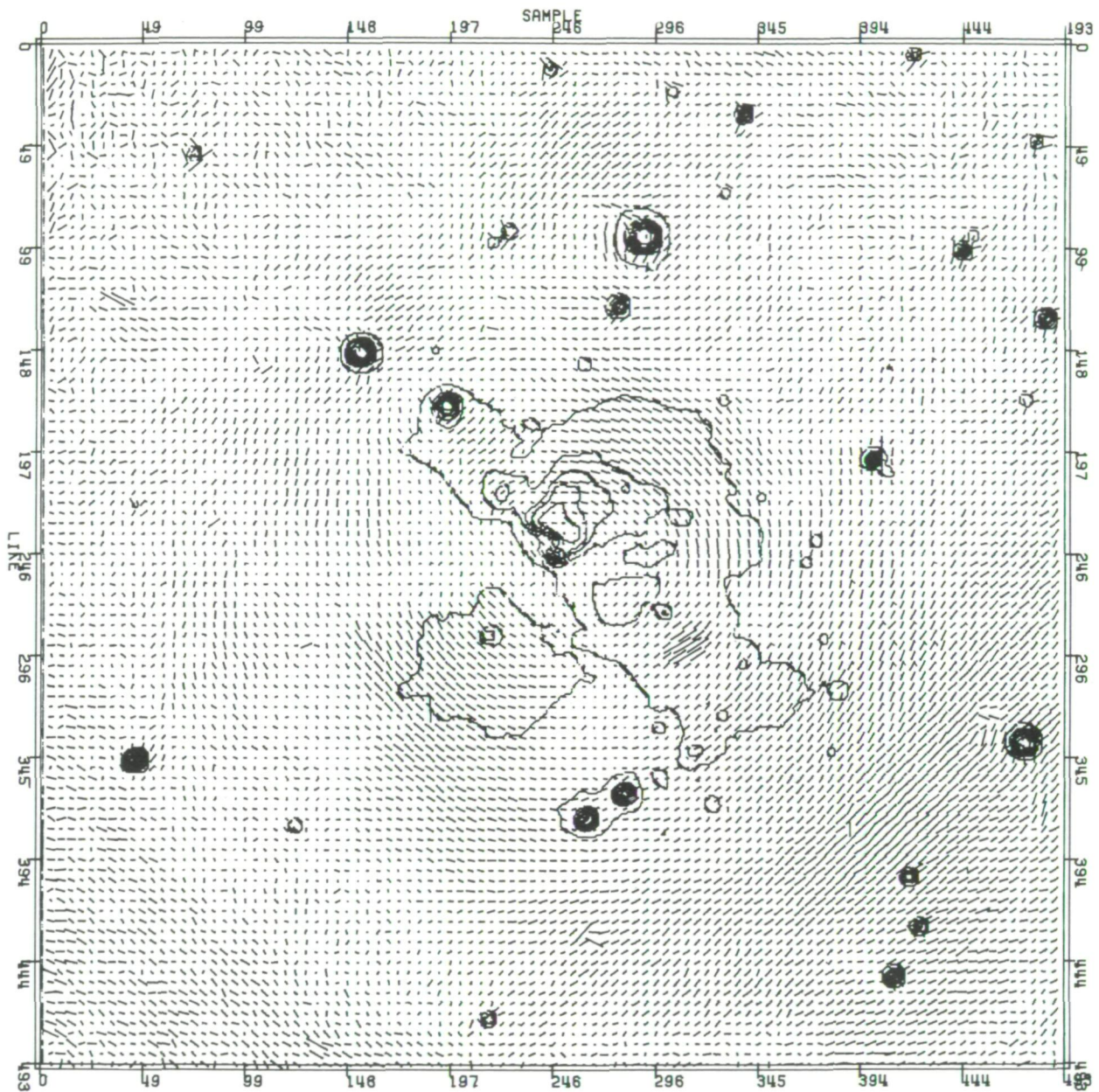


Fig. 7. Polarization picture. White corresponds to 12 percent polarization. The histograms are of the polarization, the polarization angle coded as brightness, and of the intensity (LICK H α -101)



IPL POLARIZATION MAP

LICK H-ALPHA 101 FEB 23 1976 3AJ+RG1+B1 6500 A
 RA 04 28 41 DEC 35 14 PDS SCAN 50 MIC SPOT 48 MIC SPACING 5 MET
 PLATE 7161 EXP 6 MIN POLARIZED PA= 0 DEG
 FLOT - COUNTERCLOCKWISE - F2 IN1-16

Fig. 8. Polarization direction and magnitude are displayed as vectors. Isophotes are of the intensity image (LICK H α -101)

ORIGINAL PAGE IS
 OF POOR QUALITY

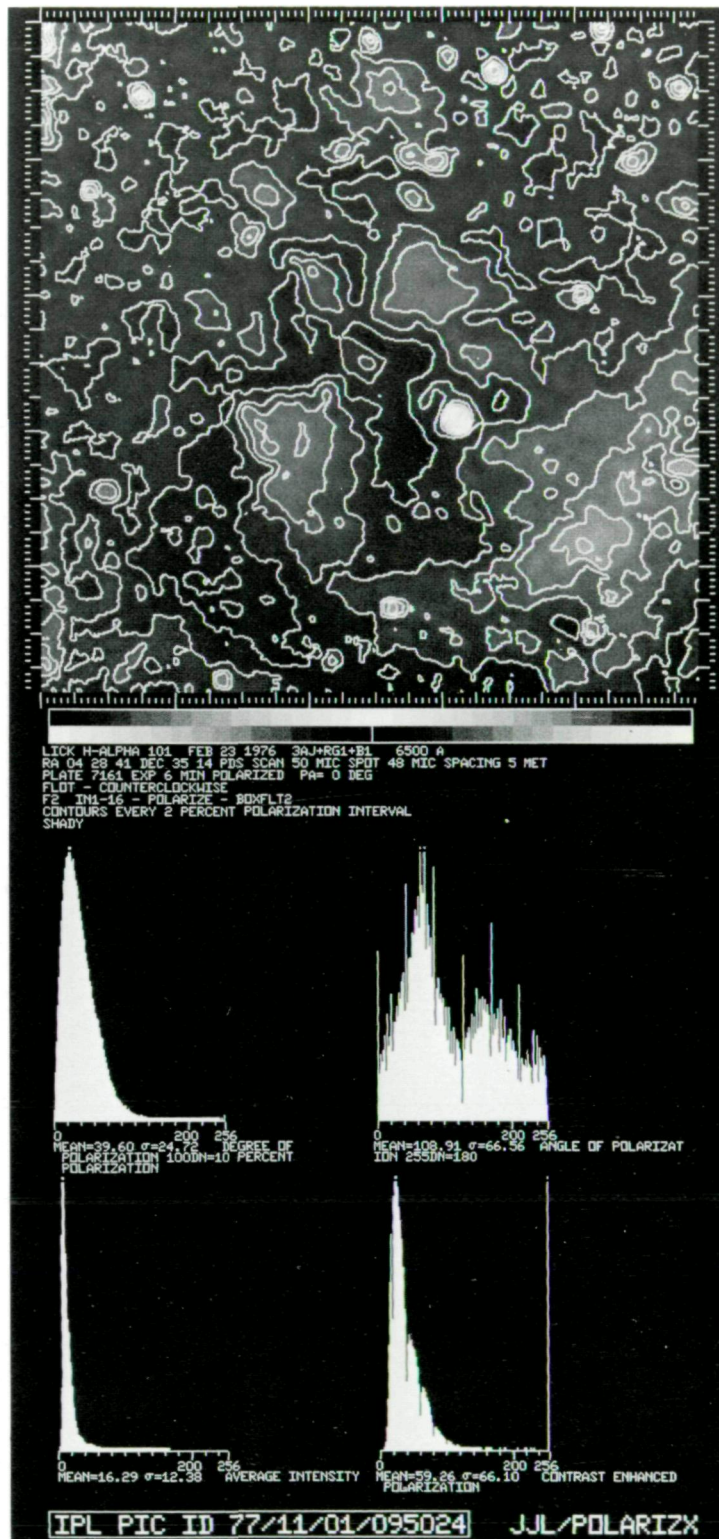


Fig. 9. Polarization isophotes are displayed on the smoothed polarization picture. Each contour signifies a 2 percent change in polarization (LICK H α -101)

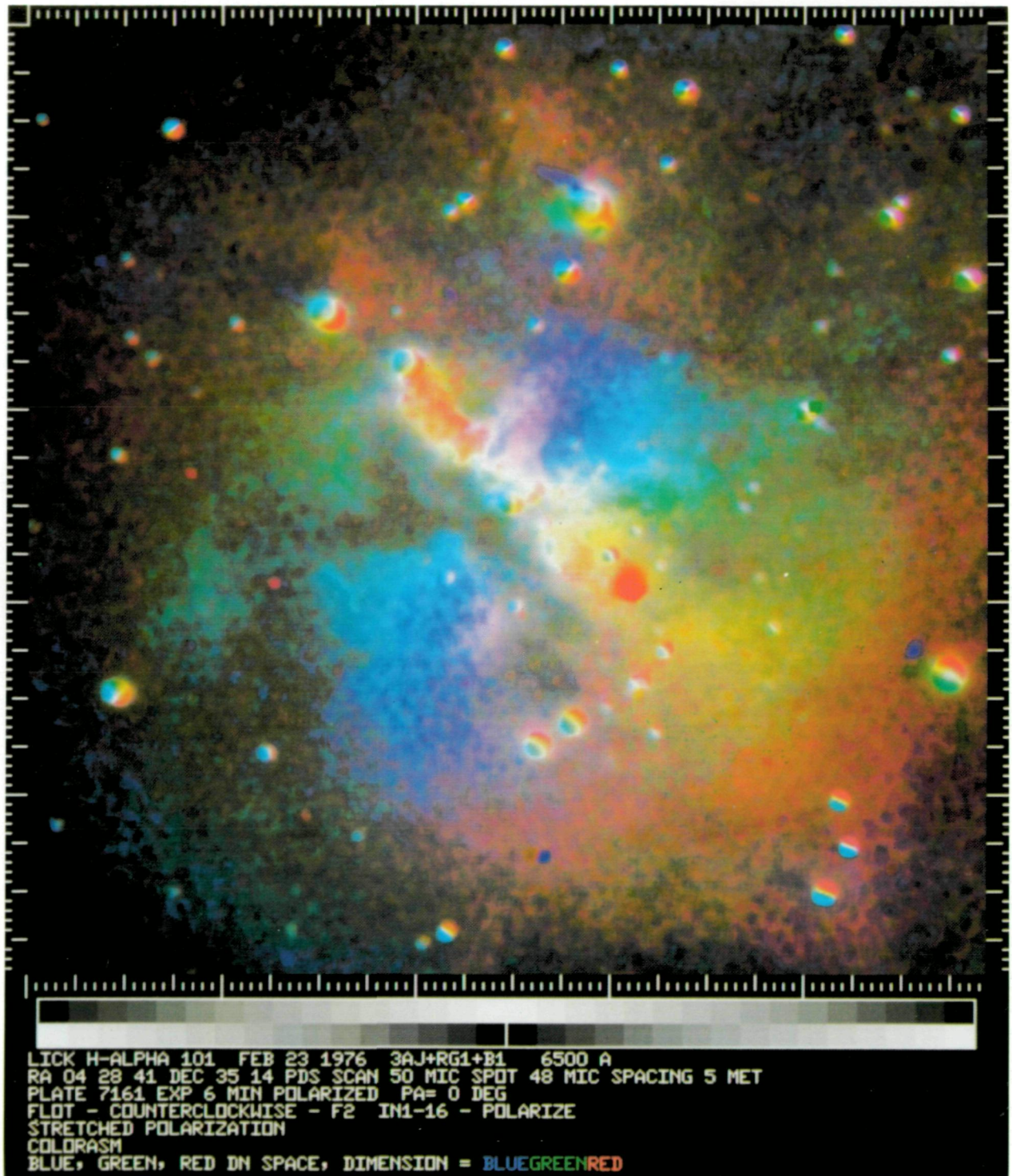
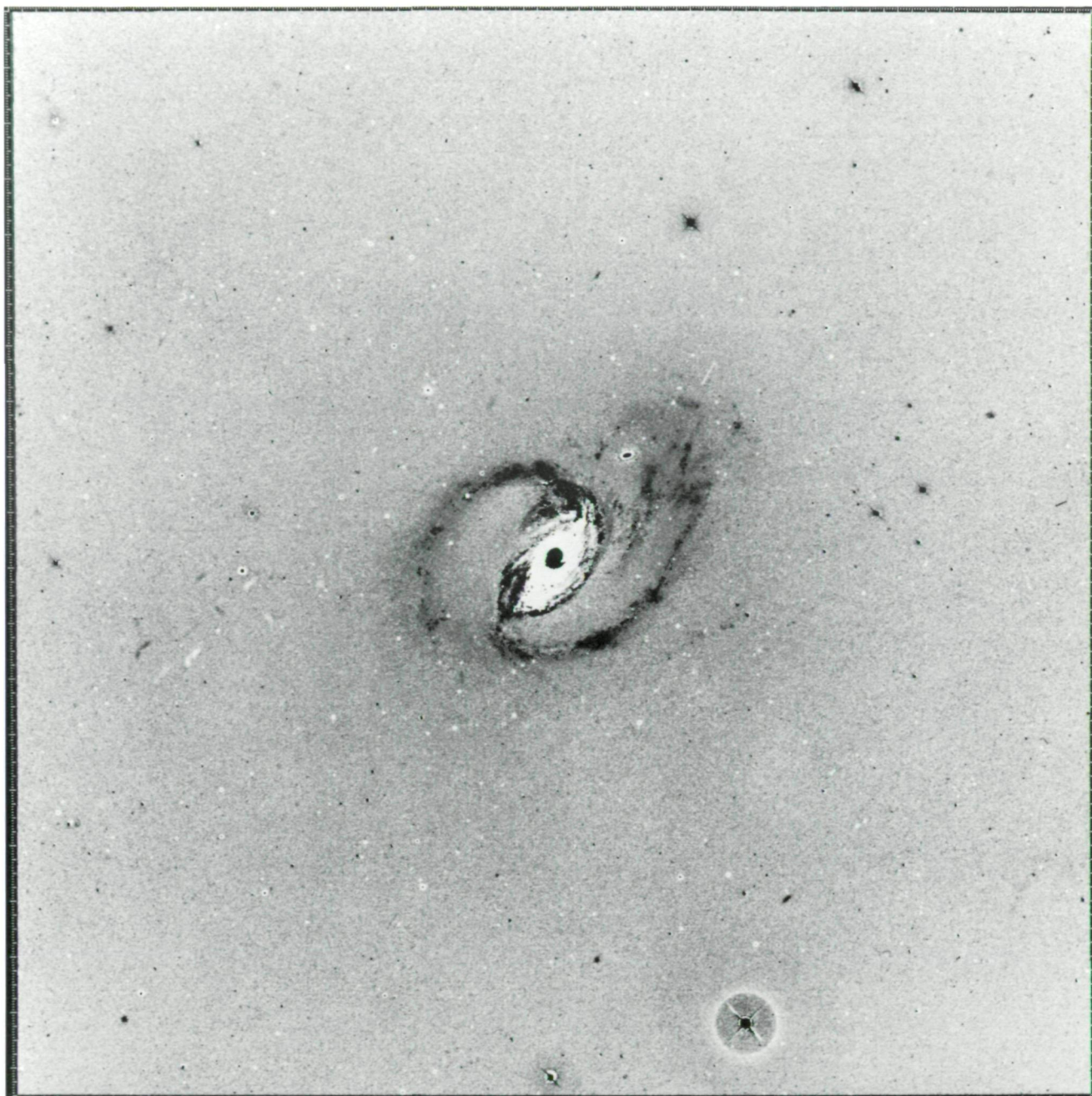


Fig. 10. Polarization coded in a color display. Intensity is coded as brightness, polarization as degree of saturation, and vector orientation as hue (LICK H α -101)

ORIGINAL PAGE IS
 OF POOR QUALITY



Fig. 11. The logarithm of the highest ranked Principal Component Transformation of four spectral bands. This image contains a weighted intensity average in which uncorrelated information and noise have been minimized (NGC1097)



NGC1097 NOV 30 1975 EXP 45 H ENUL 3AJ FILT GG385 PLATE 1381
 RA 2 45 24 DEC -30 23 (1975) 4 METER CERRO TOLDO PDS SCAN 50 MIC
 PIREGB - LINEAR
 STRETCH 0, 255, LIMITS 0, 255 - STRETCH
 FE (DIM-26, 261) #1, 2250*33, 882
 AVERAGE OF PLATES 1400 1401 1402 1403 1381
 FASTHDS
 LINEAR 05 10 77 14:56:20 MDB21
 HALF DUTY STRE 0 511
 LINEAR - STRETCH 0, 511, LIMITS 0, 255
 SAR 05 10 77 15:29:53 MDB21
 MSS - V2
 ASTRICH2
 STRETCH 92-127

EIGCOLDX SAT JUN 11, 1977 044822 JPL/IPL

Fig. 12. The second ranked Principal Component Transformation of four spectral bands. This image contains the dominant color differences only in which no intensity information is present (NGC1097)



Fig. 13. The third ranked Principal Component Transformation of four spectral bands. This image contains less highly correlated color differences (NGC1097)



Fig. 14. The fourth or lowest Principal Component Transformation of four spectral bands. This image contains that information which is uncorrelated between the four original bands. Most of the information visible is noise and plate mottling (NGC1097)

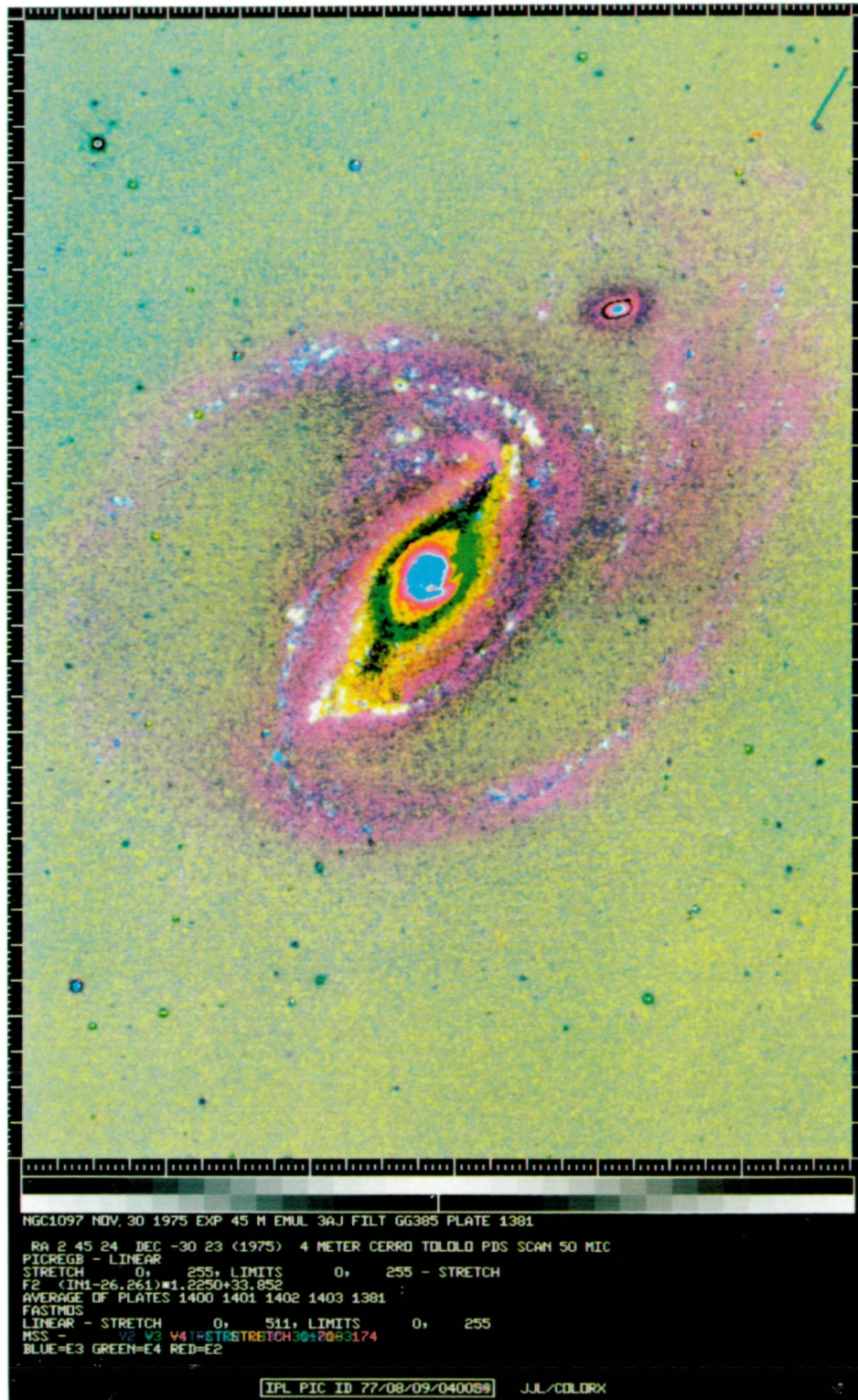


Fig. 15. A color composite image produced by adding the three color coded lowest Principal Component Transformations (NGC1097)

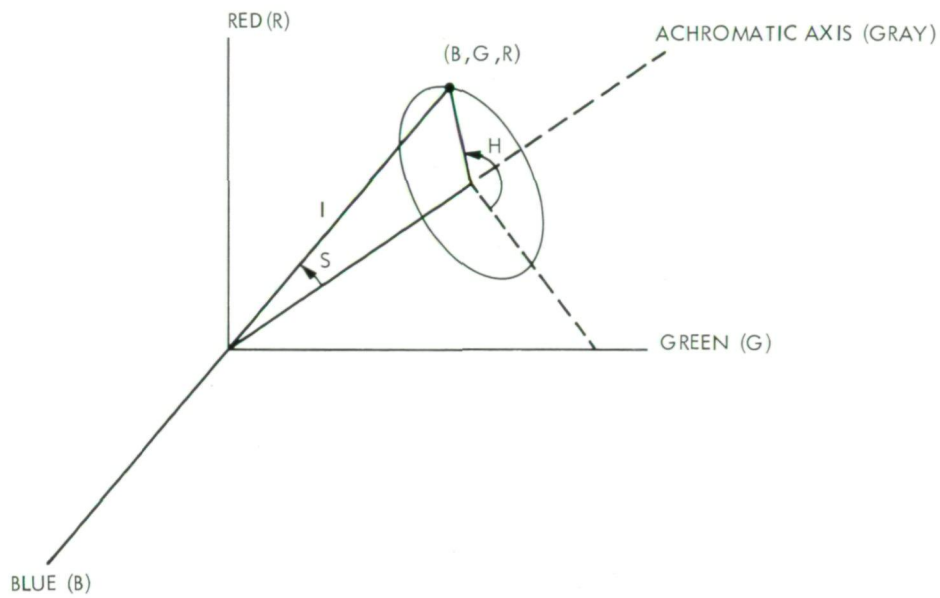


Fig. 16. The idealized coordinate system relating blue, green, and red cartesian coordinates with hue, saturation, and intensity polar coordinates

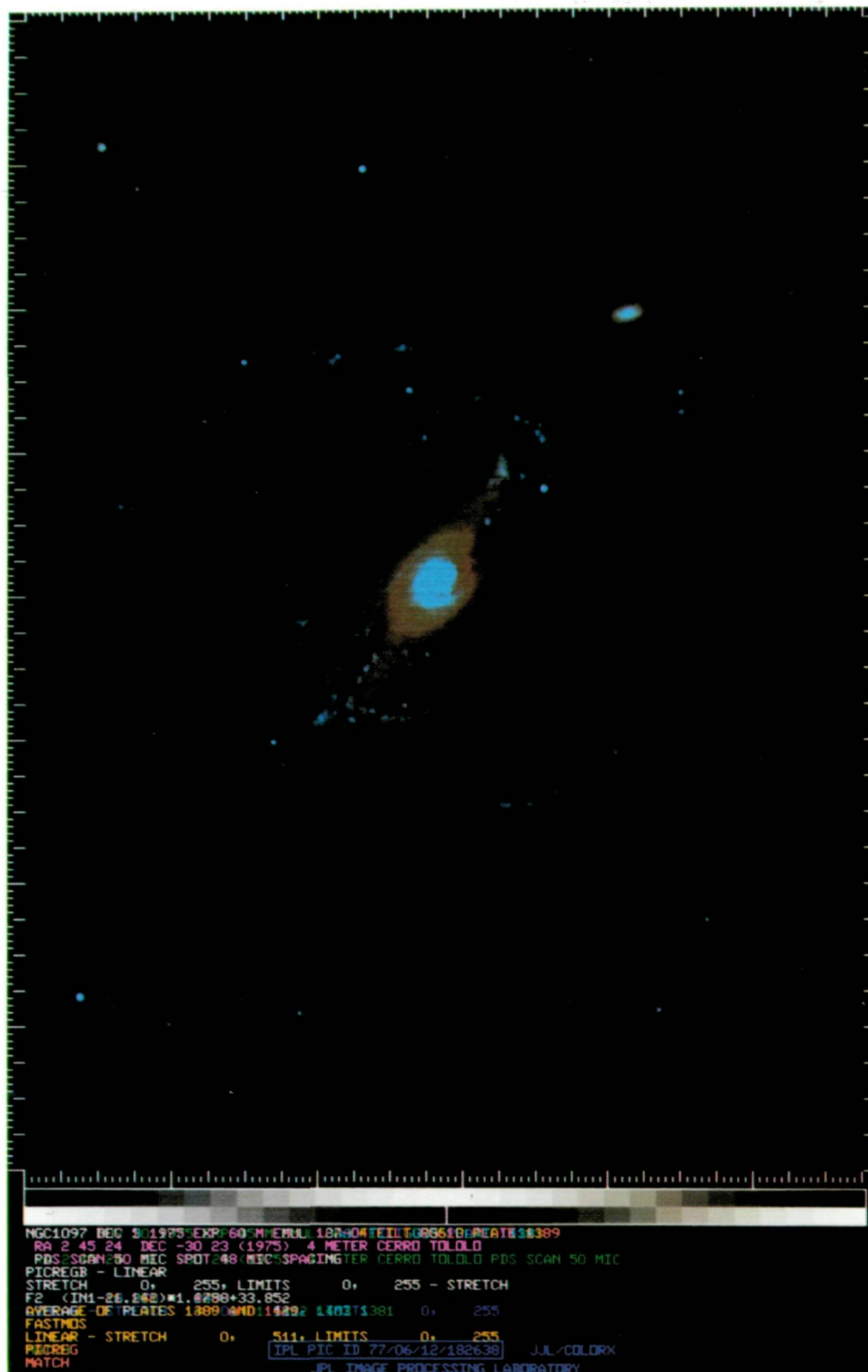


Fig. 17. Color reconstruction produced by combining blue = 103a0, green = IIIaJ, and red = 127-04 in a purely additive manner. Colors are discriminated only poorly by the eye.

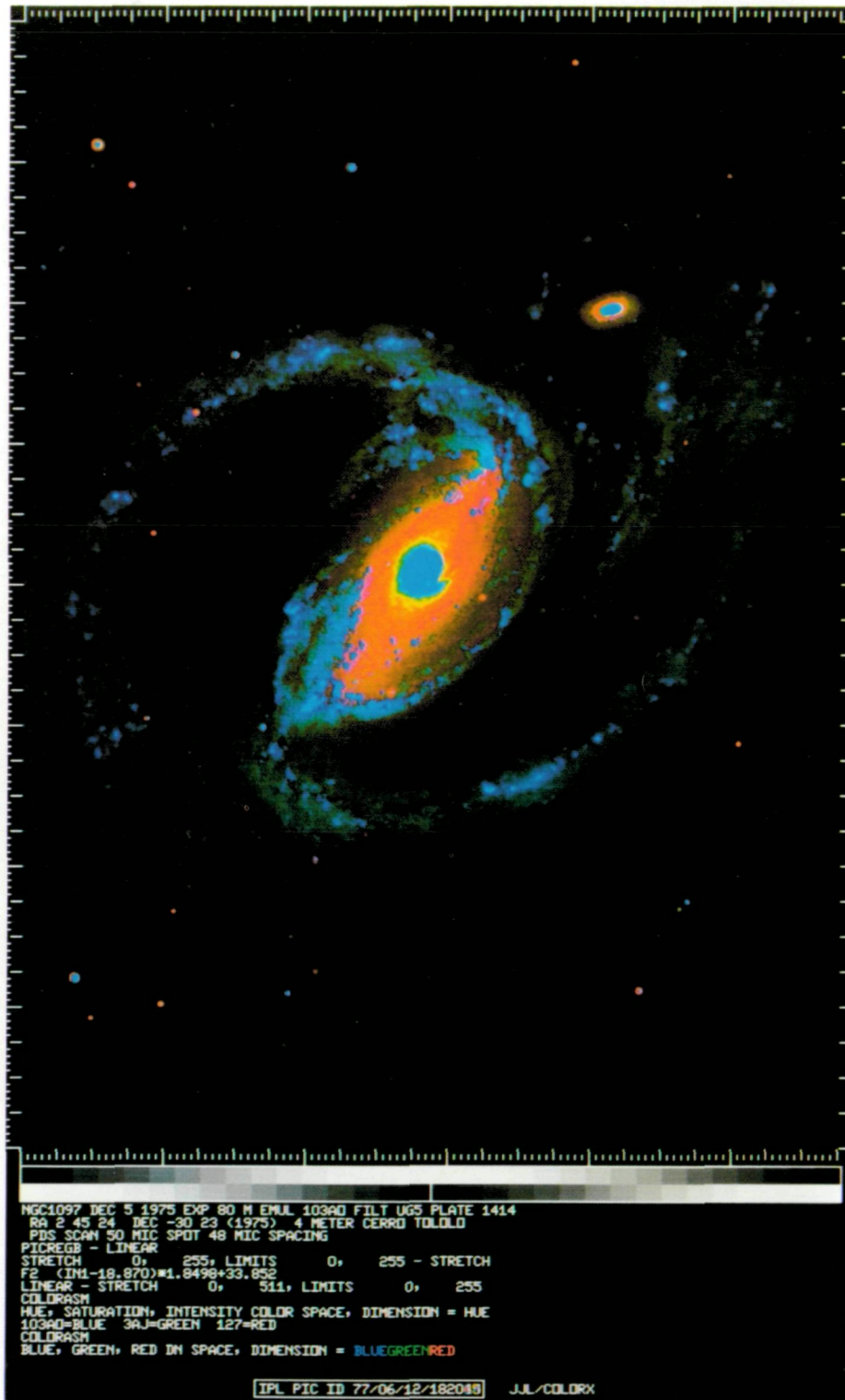


Fig. 18. Saturation enhanced color reconstruction. The same images used to produce Figure 17 were transformed to the HSI space and the saturation picture was contrast enhanced. Transforming back to blue, green, and red produces a color enhanced image where the colors are more readily recognized. The hues have not been altered (NGC1097)

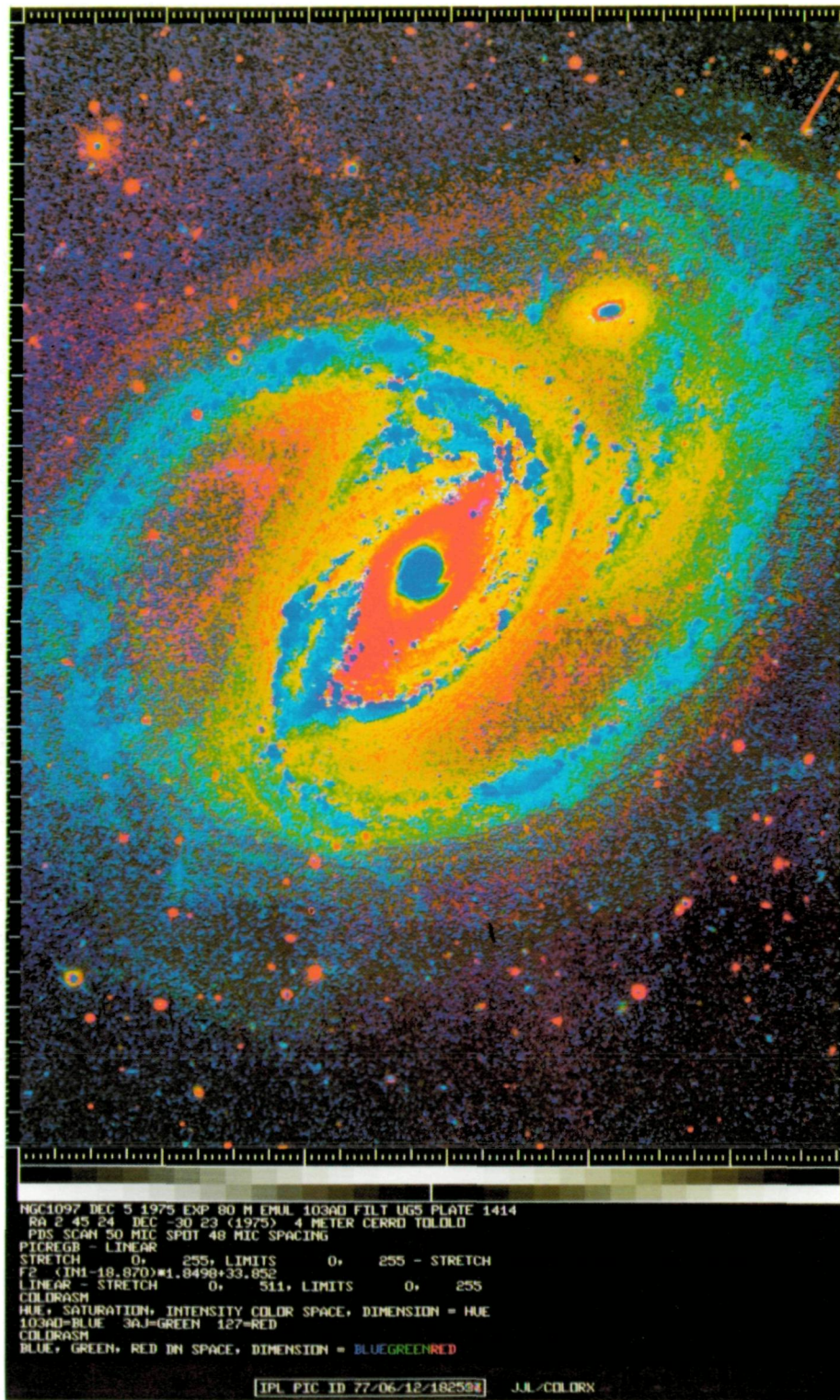


Fig. 19. Saturation enhanced color reconstruction. The same images as Figure 18 were used except that before the inverse transformations was made to blue, green, and red, the intensity image was replaced by its logarithm. Discriminability is now nearly complete (NGC1097)

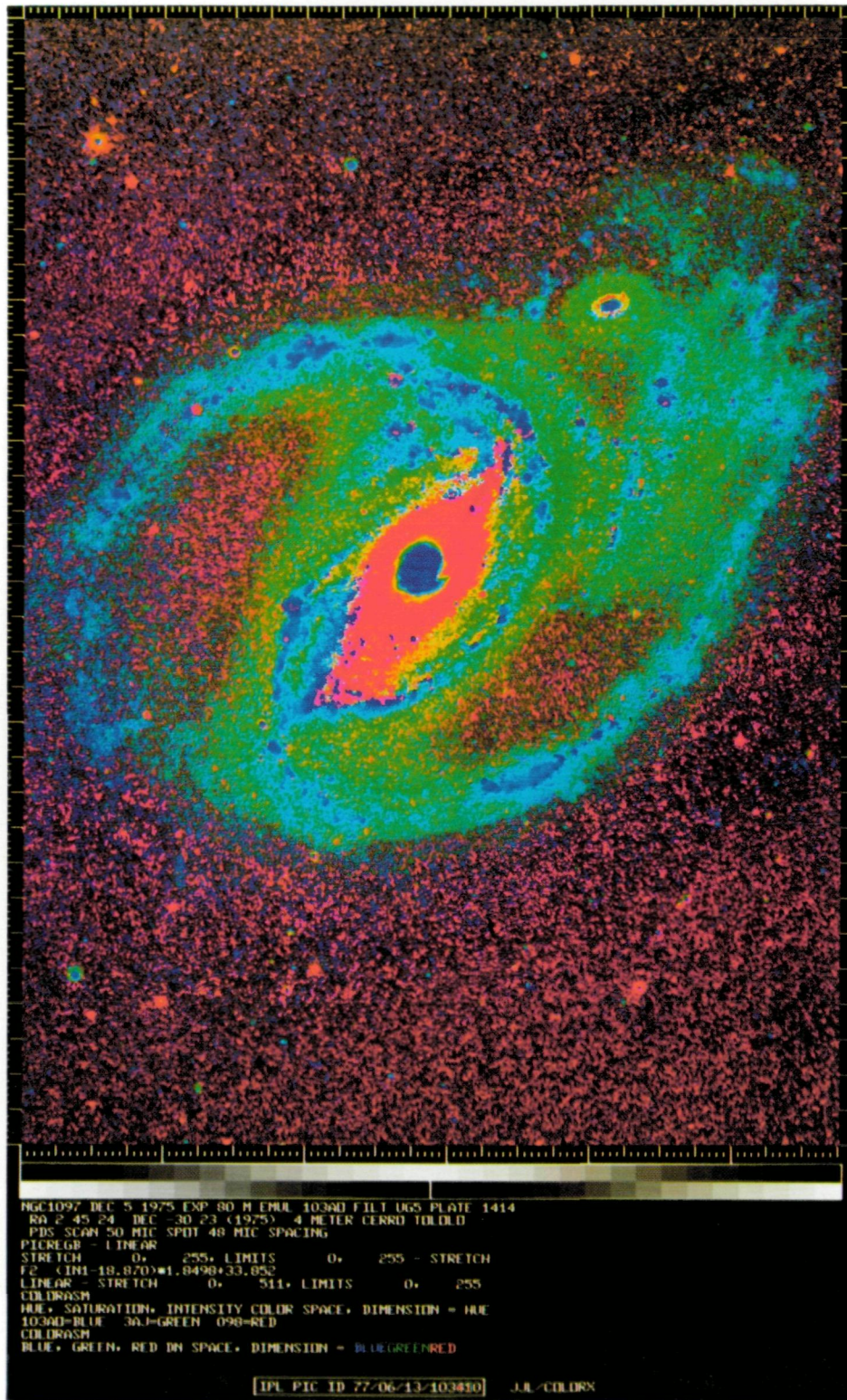


Fig. 20. Color enhanced picture with blue = 103a0, green = IIIaJ, and red = 098. Both log intensity and contrast enhanced saturation have been performed (NGC1097)

ORIGINAL PAGE IS
OF POOR QUALITY

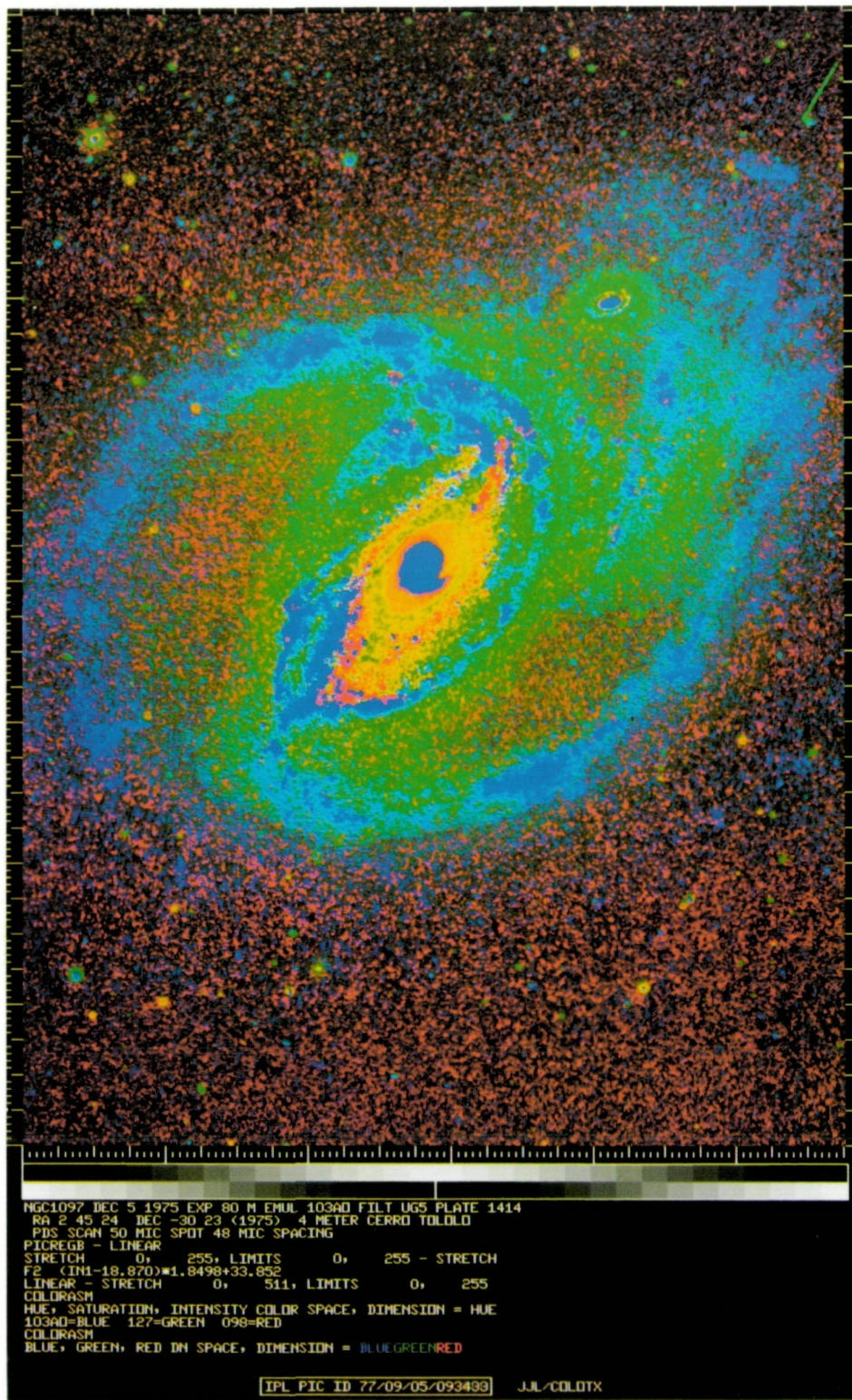


Fig. 21. Color enhanced picture with blue = 103a0, green = 127-04, and red = 098. Both log intensity and contrast enhanced saturation have been performed (NGC1097)

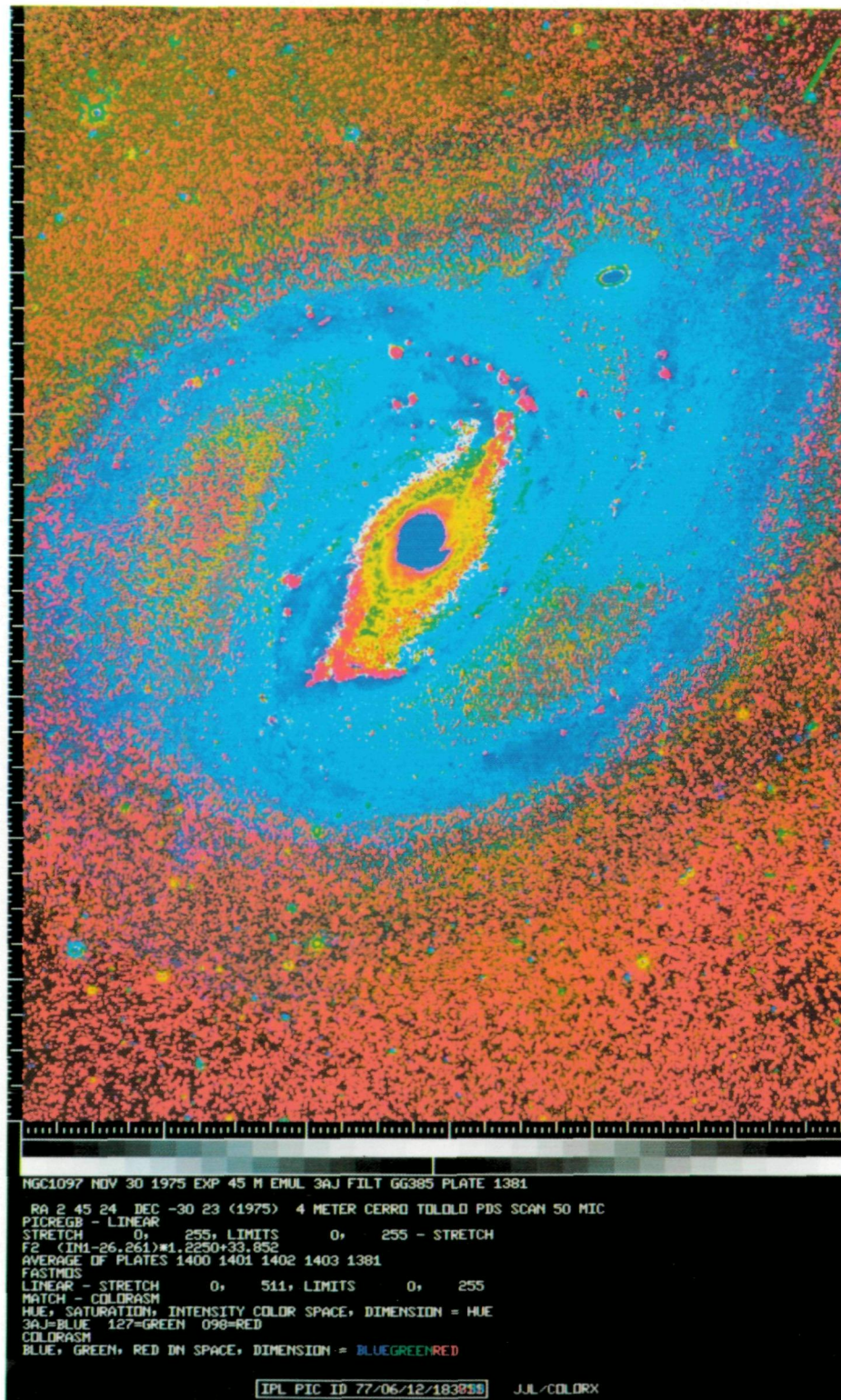


Fig. 22. Color enhanced picture with blue = IIIaJ, green = 127-04, and red = 098. Both log intensity and color enhanced saturation have been performed (NGC1097)

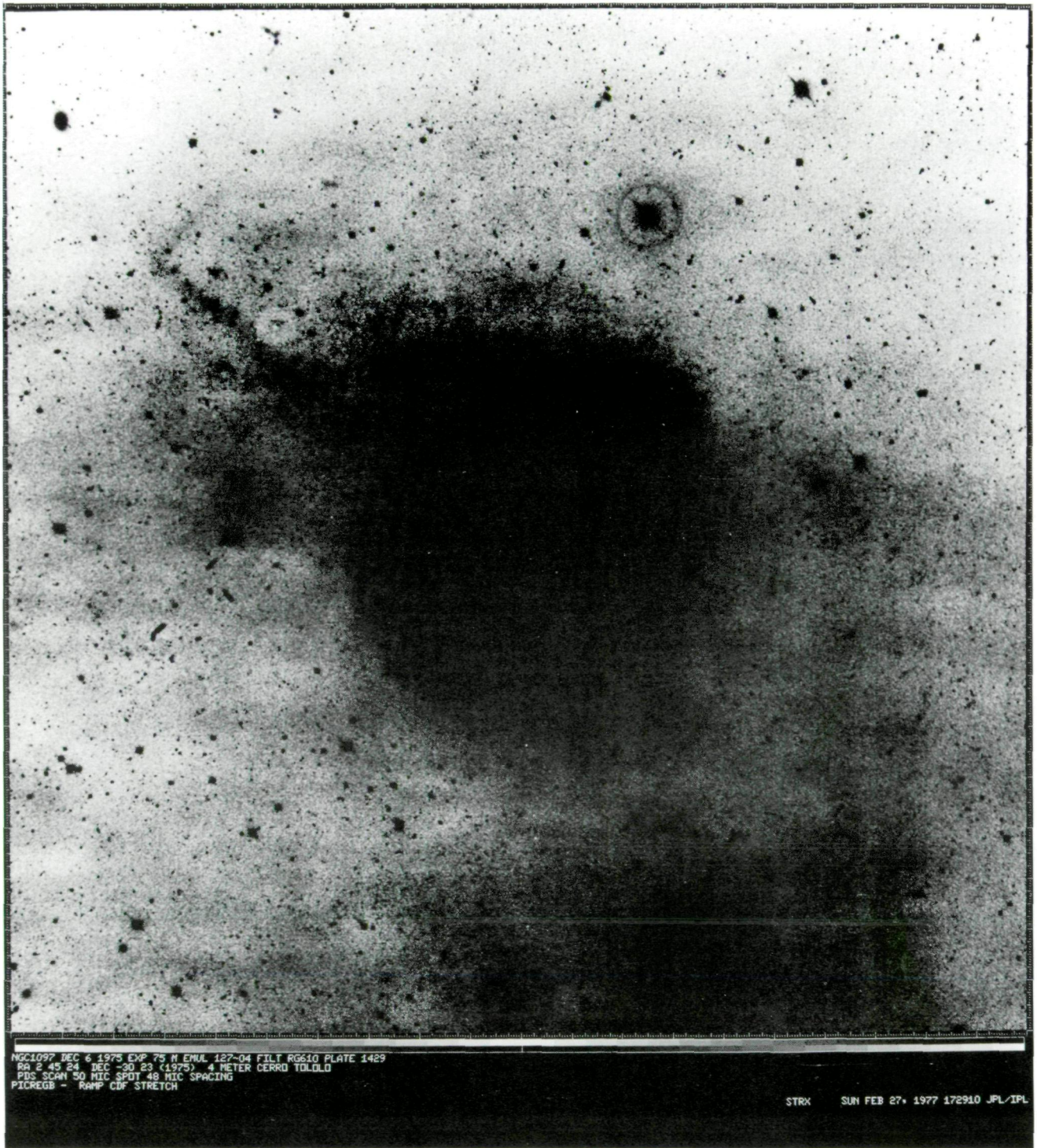


Fig. 23. Contrast enhanced picture of a single 127-04 plate. Plate mottling is sufficiently severe to mask much of the information in the image (NGC1097)

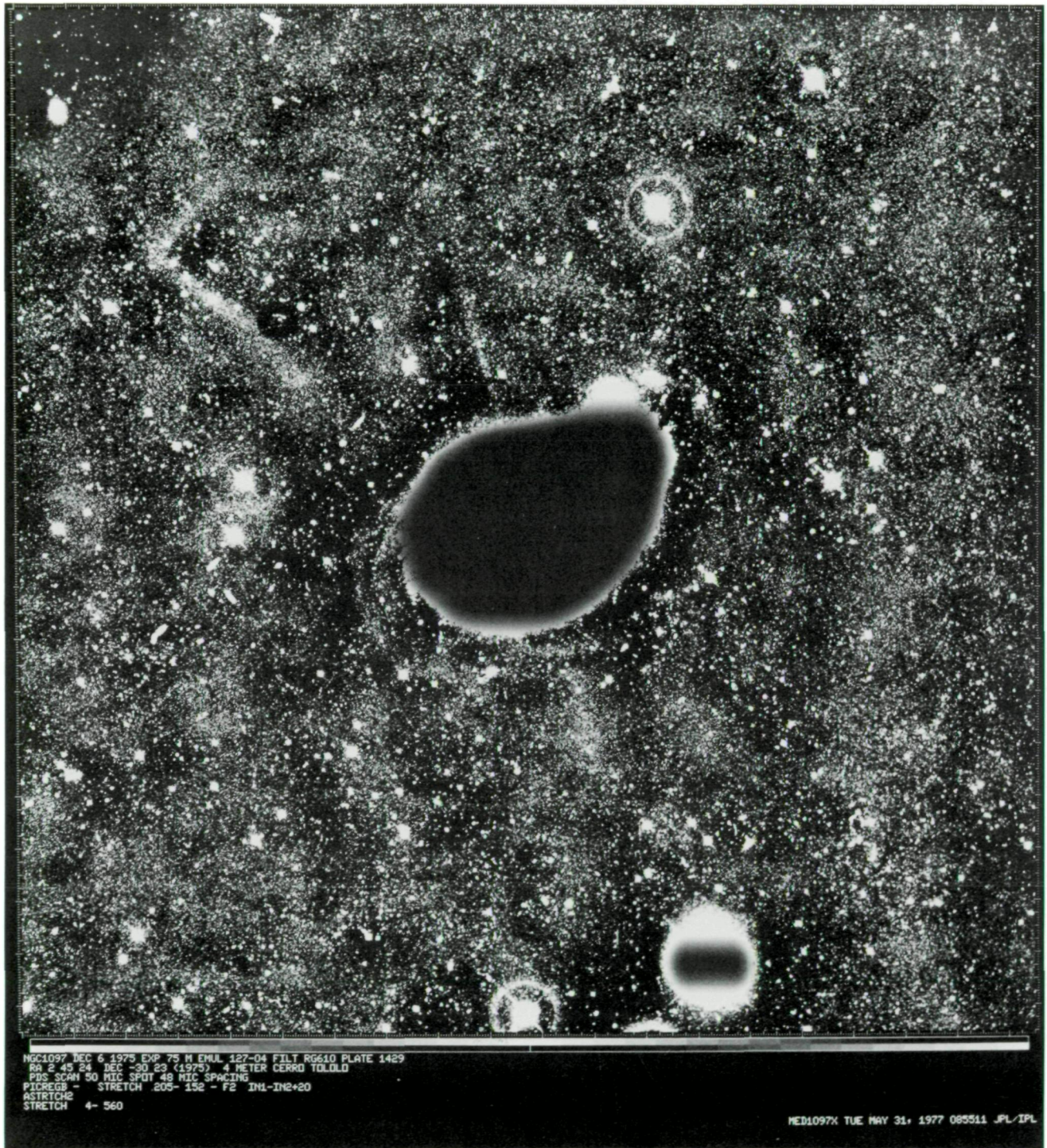


Fig. 24. Background flattened image. This is the same plate as Figure 23 after processing with a one-dimensional Median filter. Faint structure in the plate background can be discerned now that much of the large scale mottling has been suppressed (NGC1097)

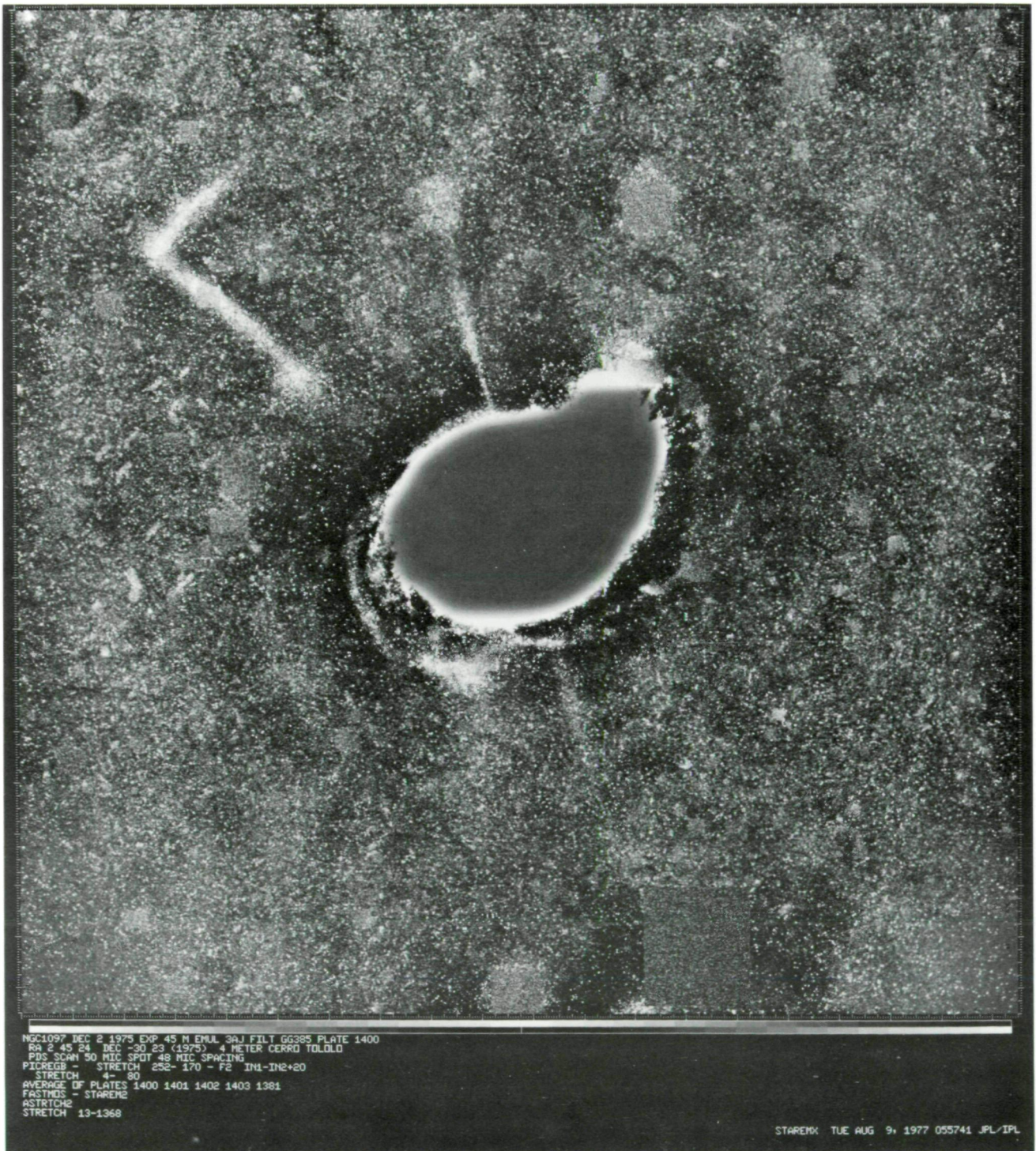


Fig. 25. The average of five IIIaJ plates has been processed to remove all of the larger stellar and galaxy images. Jets emanating from NGC1097 can be more readily observed (NGC1097)

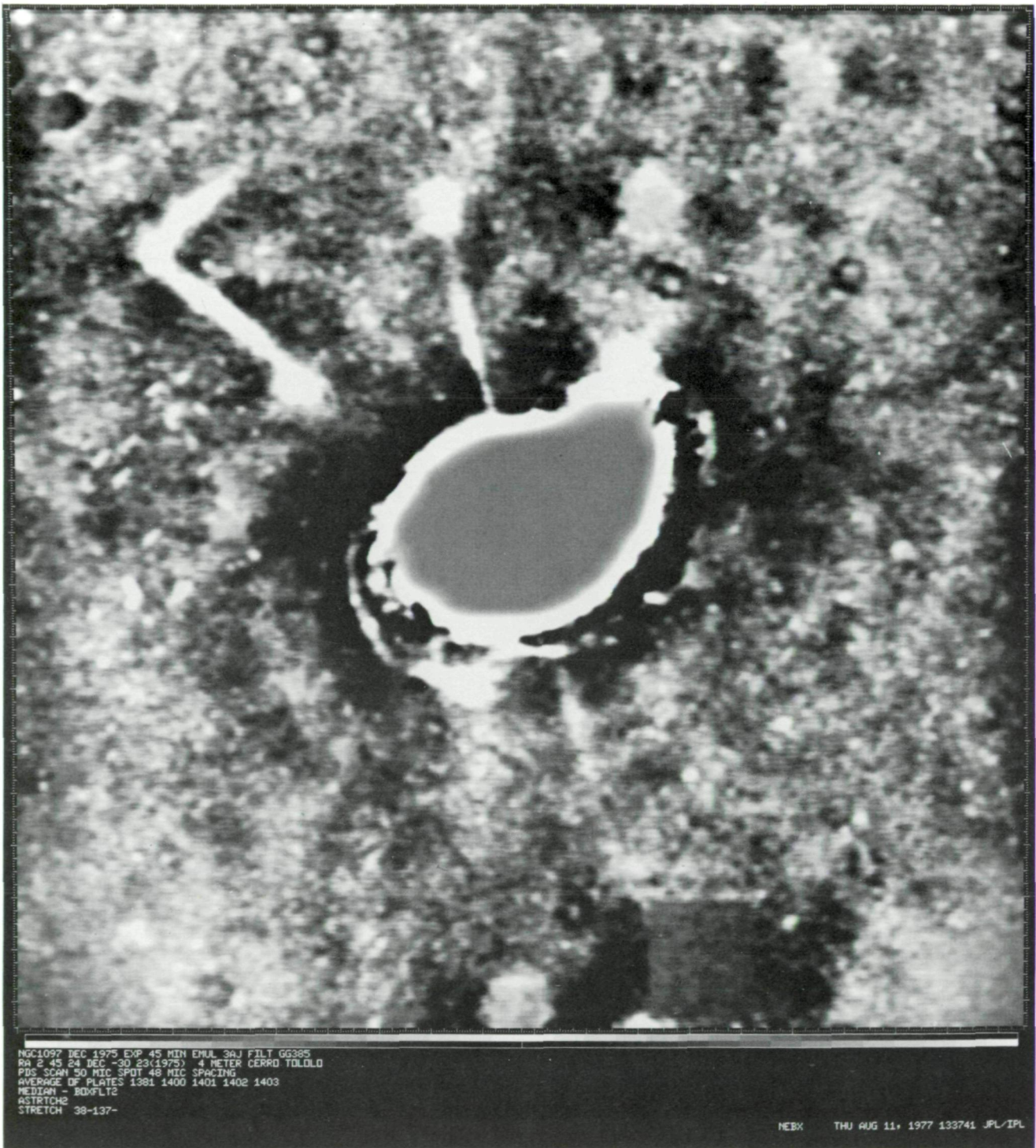


Fig. 26. The image in Figure 25 has been processed with a small Median filter to suppress small stellar images and plate grain (NGC1097)

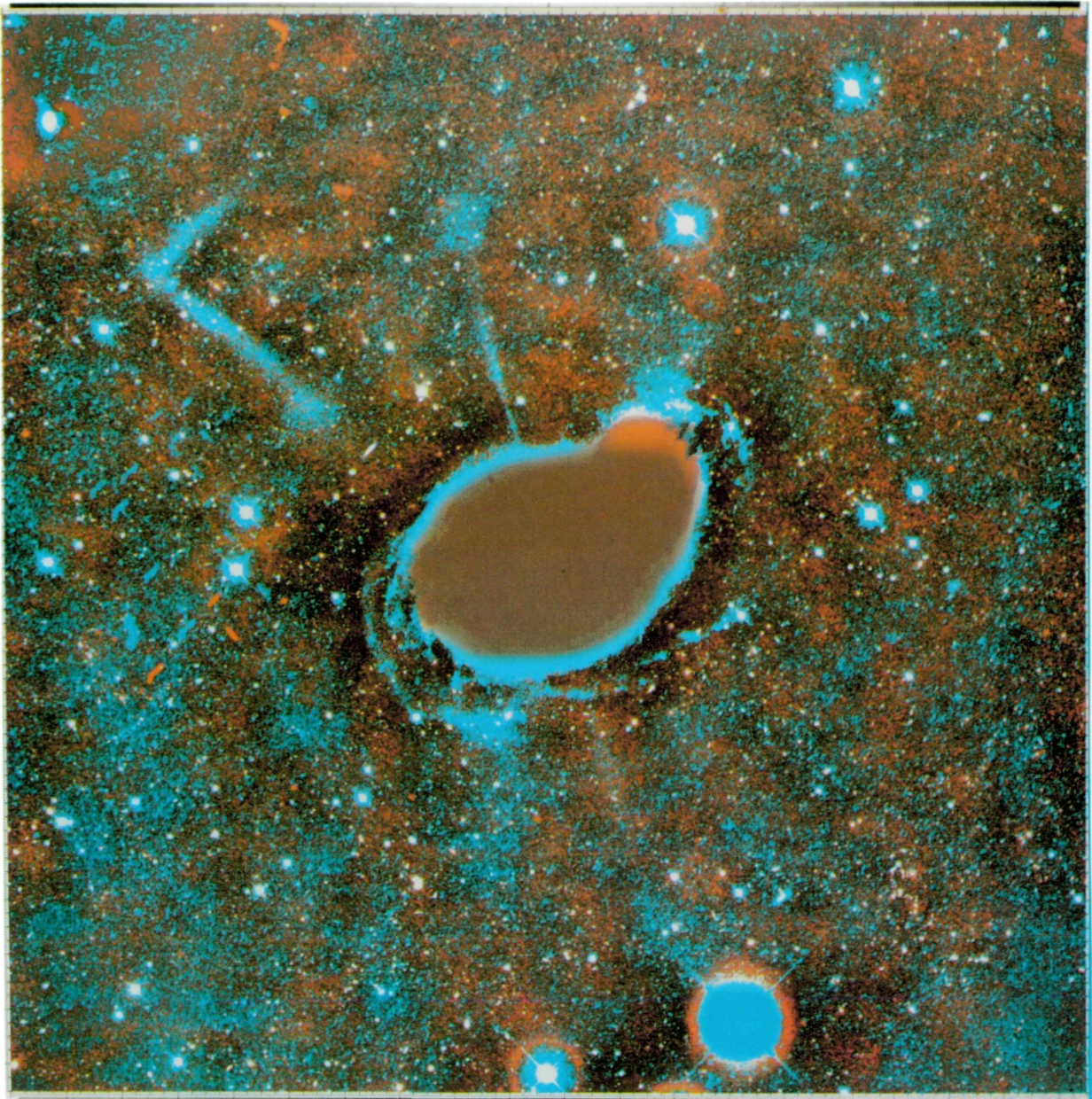


Fig. 27. Color reconstruction using two stacks of flattened pictures. Blue = IIIaJ, and red = 127-04. Saturation enhancement was performed to reveal color differences in the jets (NGC1097)

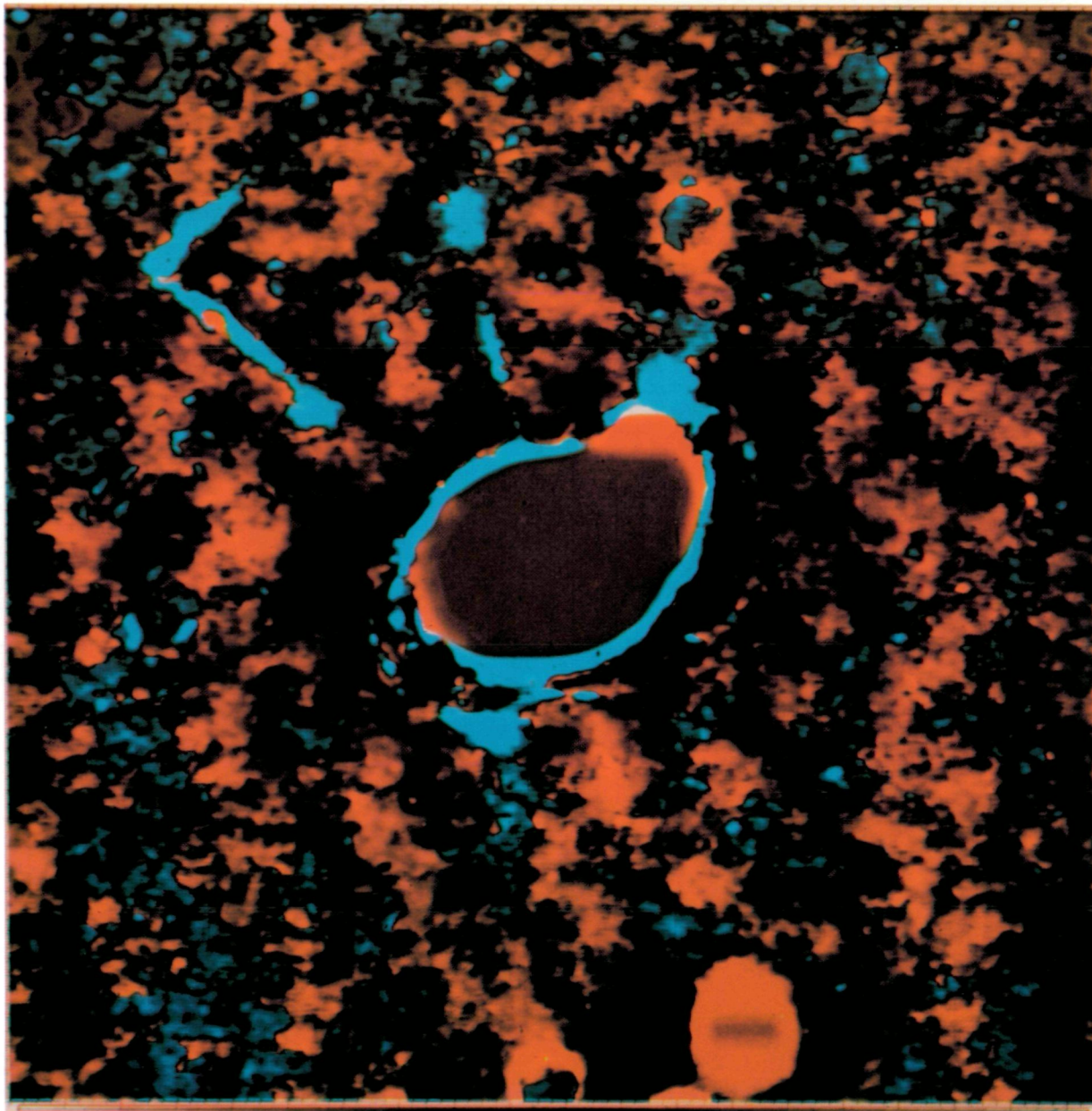


Fig. 28. The image in Figure 27 was modified by removing small stellar and grain structure with a small Median filter (NGC1097)

ORIGINAL PAGE IS
OF POOR QUALITY

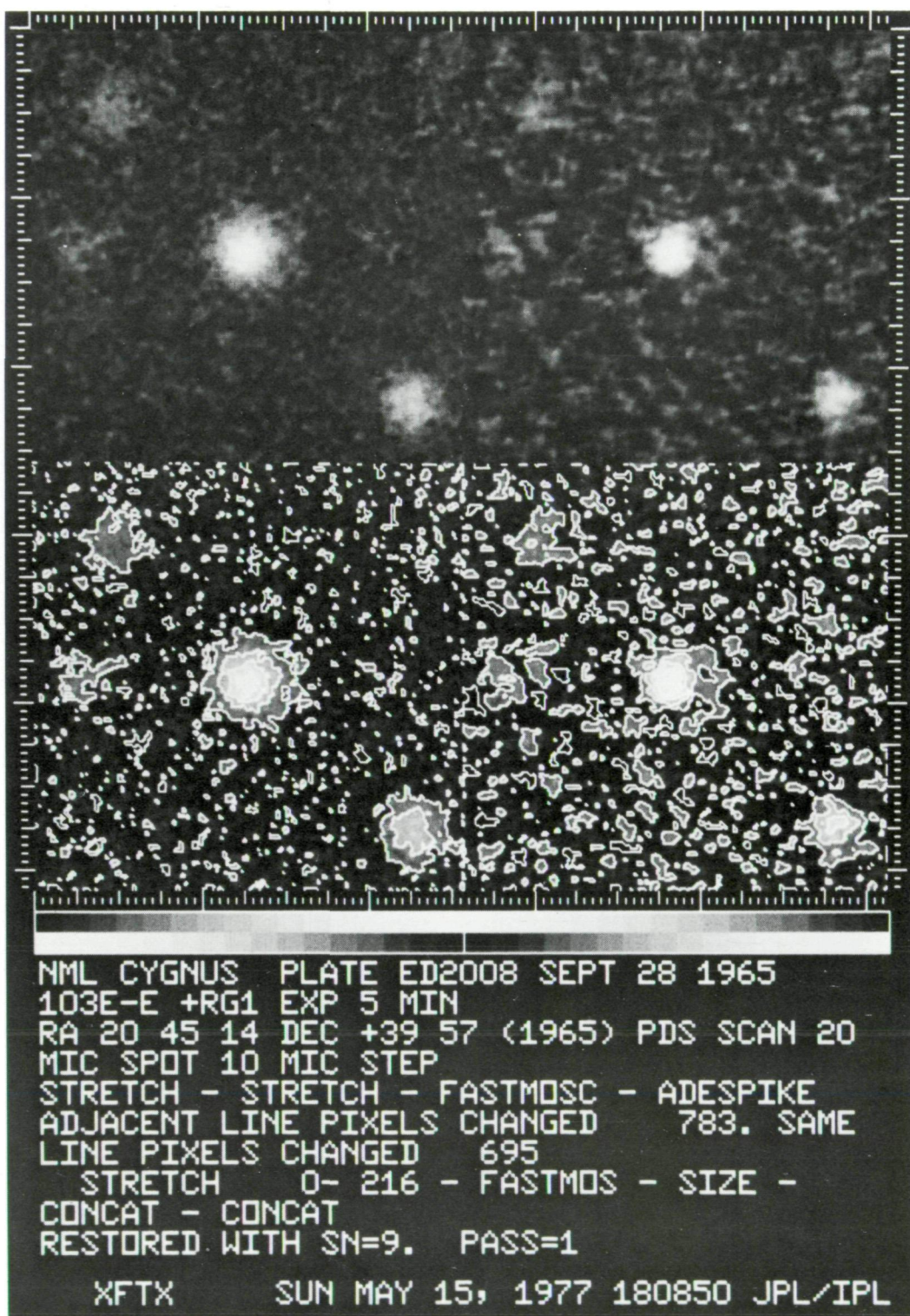


Fig. 29. Deconvolution to compensate for atmospheric seeing. Top left is the original image and top right is the deconvolved image. The bottom row is the same as the top row with isophotes superimposed. A reference star has been inserted into the lower right corner of each quadrant (NML Cygnus)

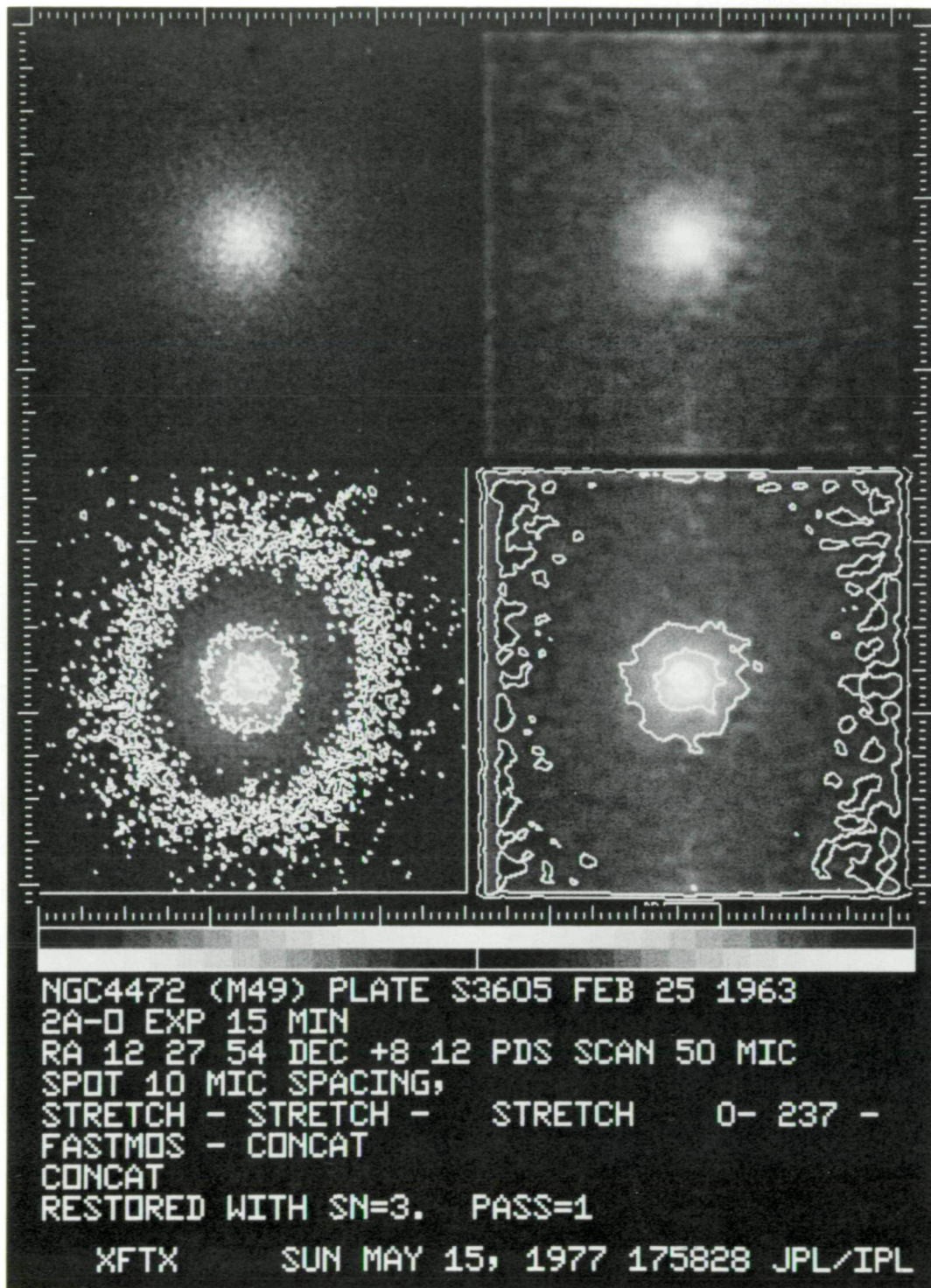


Fig. 30. Deconvolution of the nuclear region of an elliptical galaxy in the same mosaic format as Figure 29 (NGC4472)

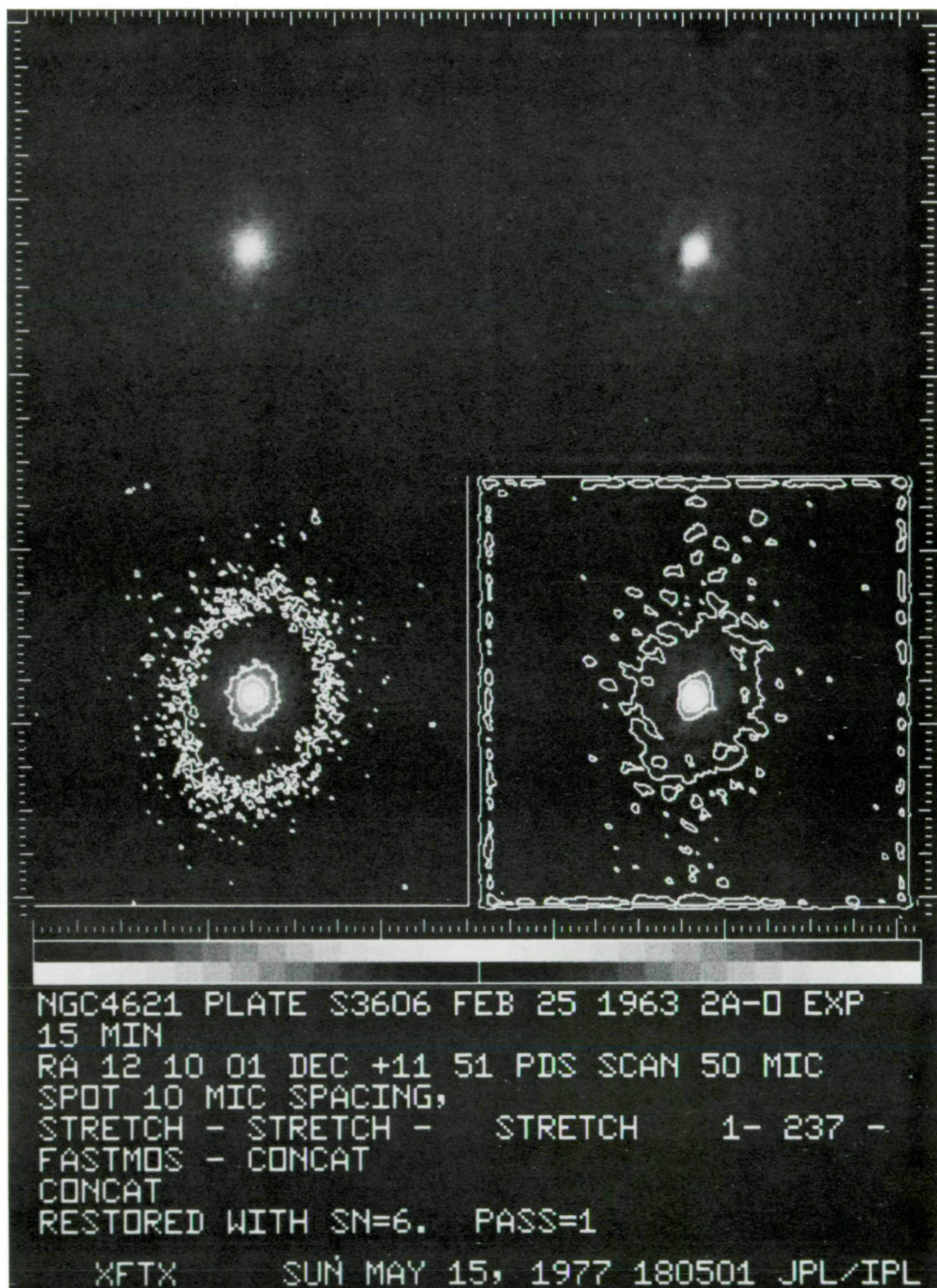


Fig. 31. Deconvolution of an elliptical galaxy nucleus (NGC4621)

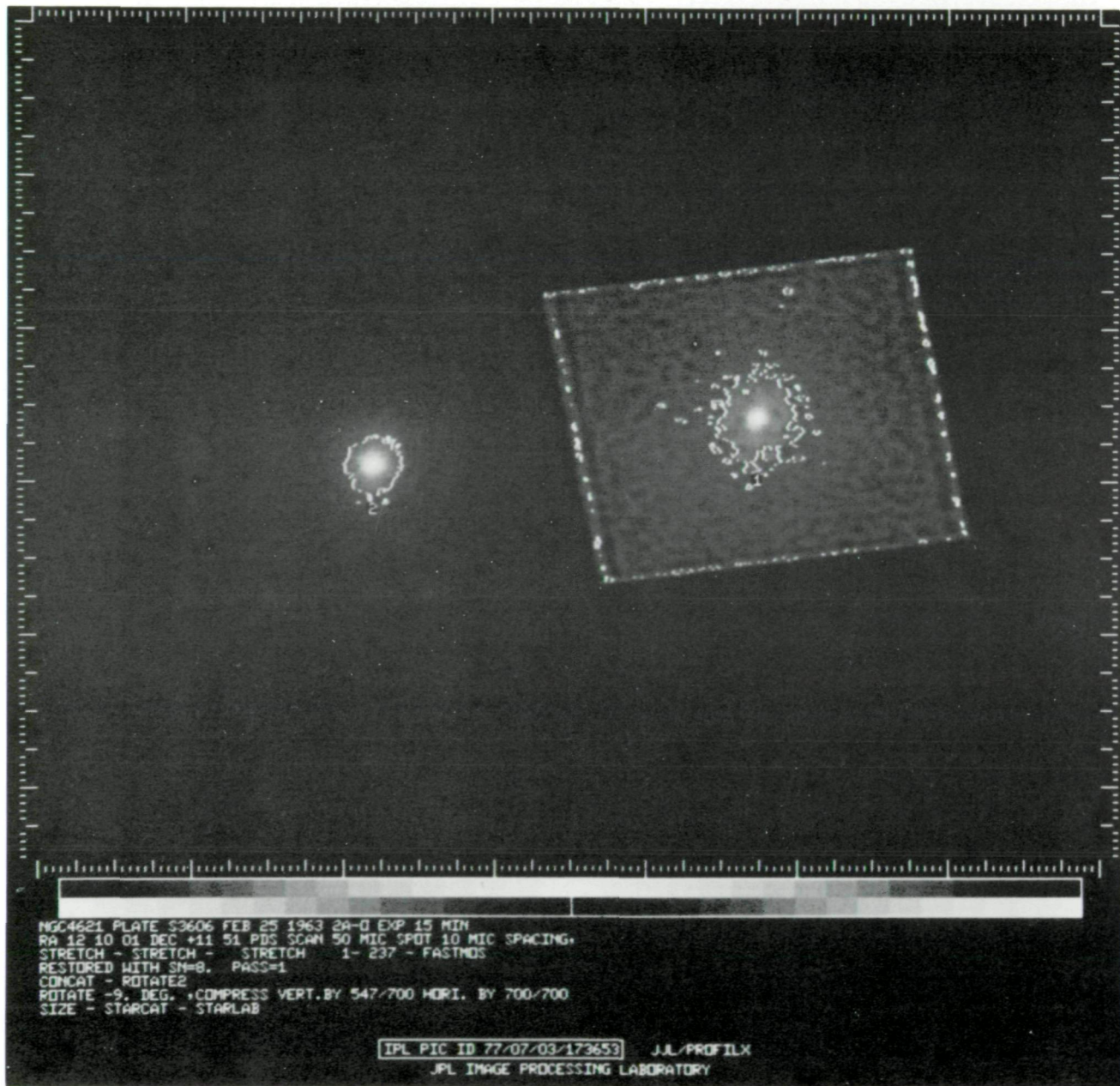


Fig. 32. Geometrically rectified mosaic of before deconvolution (left) and after deconvolution (right) to remove ellipticity caused by viewing geometry (NGC4621)

**ORIGINAL PAGE IS
OF POOR QUALITY**

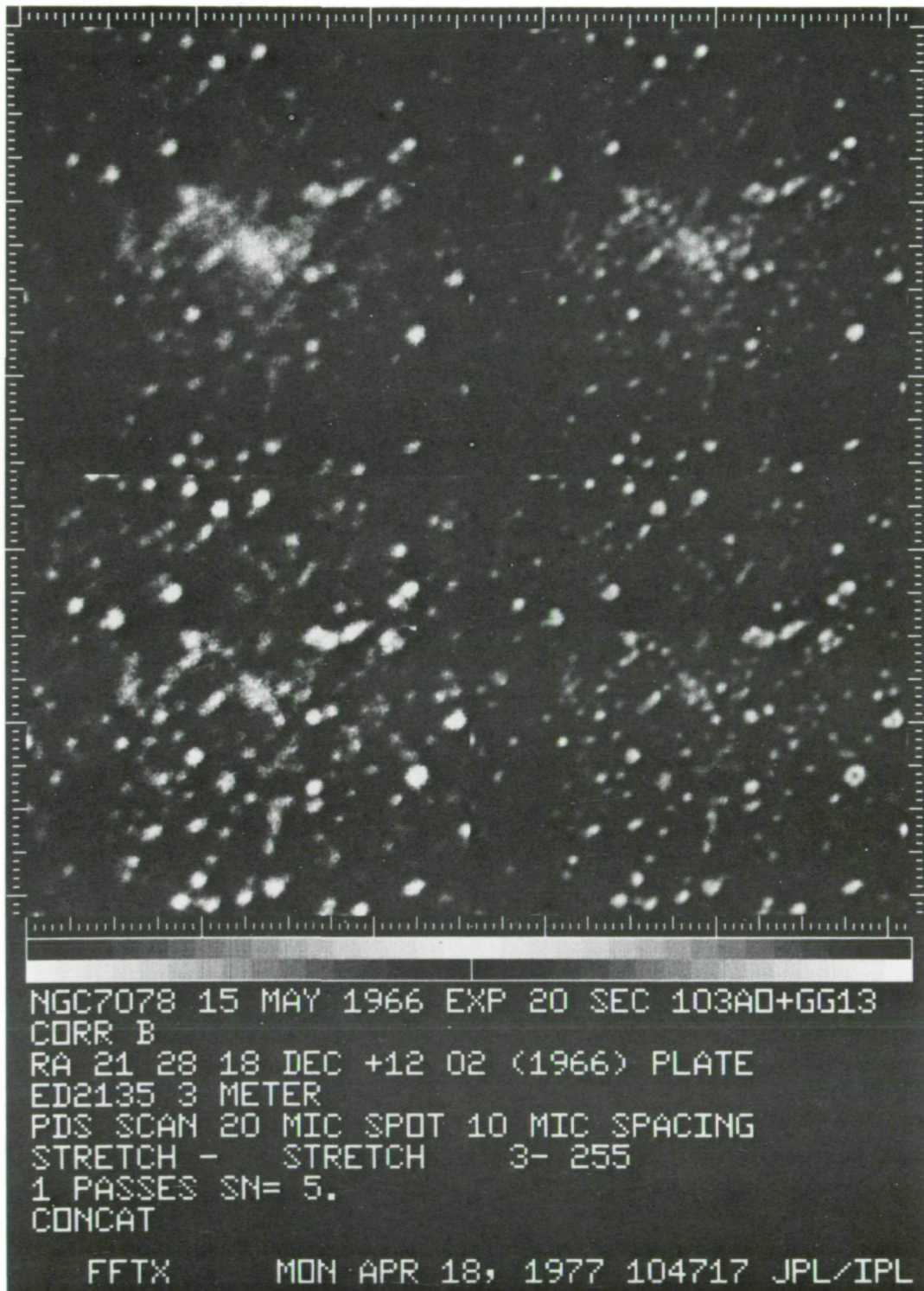


Fig. 33. Mosaic of images of the central region of a globular cluster. Top left is the original blurred image. Top right is the deconvolved image. Bottom left is the blurred image after removal of the global object shape. Bottom right is the deconvolved image of the one to its left. Some resolution improvement is apparent (NGC7078)

ORIGINAL PAGE IS
OF POOR QUALITY

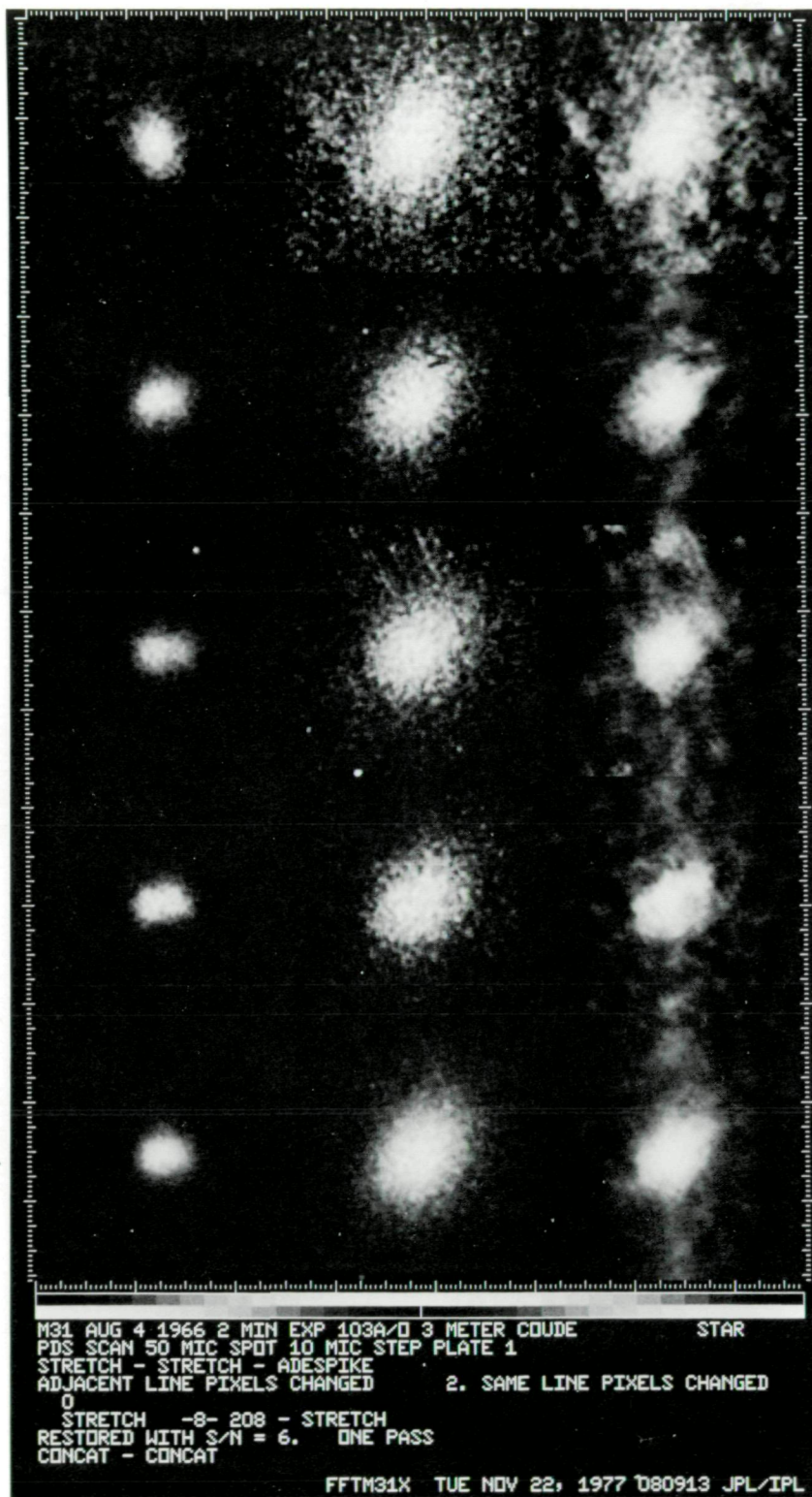


Fig. 34. Mosaic of the nucleus of M31. Each of the top four rows represent a separate plate. The left image is a reference star, the middle image is the blurred nucleus, and the right image is the deconvolved nucleus. The bottom row is the average of the top four rows (M31)

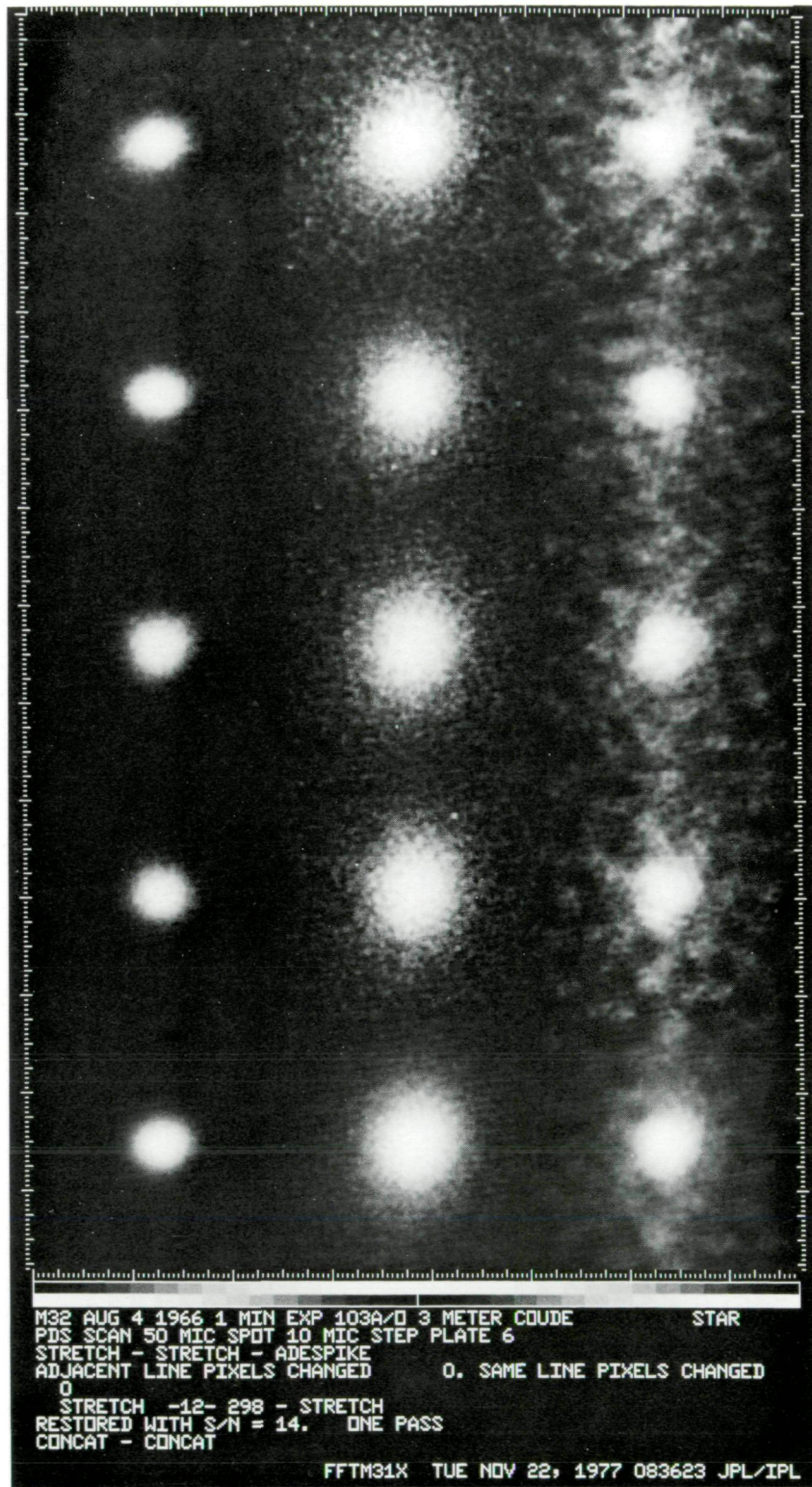


Fig. 35. Mosaic of the nucleus of M31 in the same format as Figure 34. A higher signal to noise ratio enabled more complete deconvolution than in Figure 34 (M32)

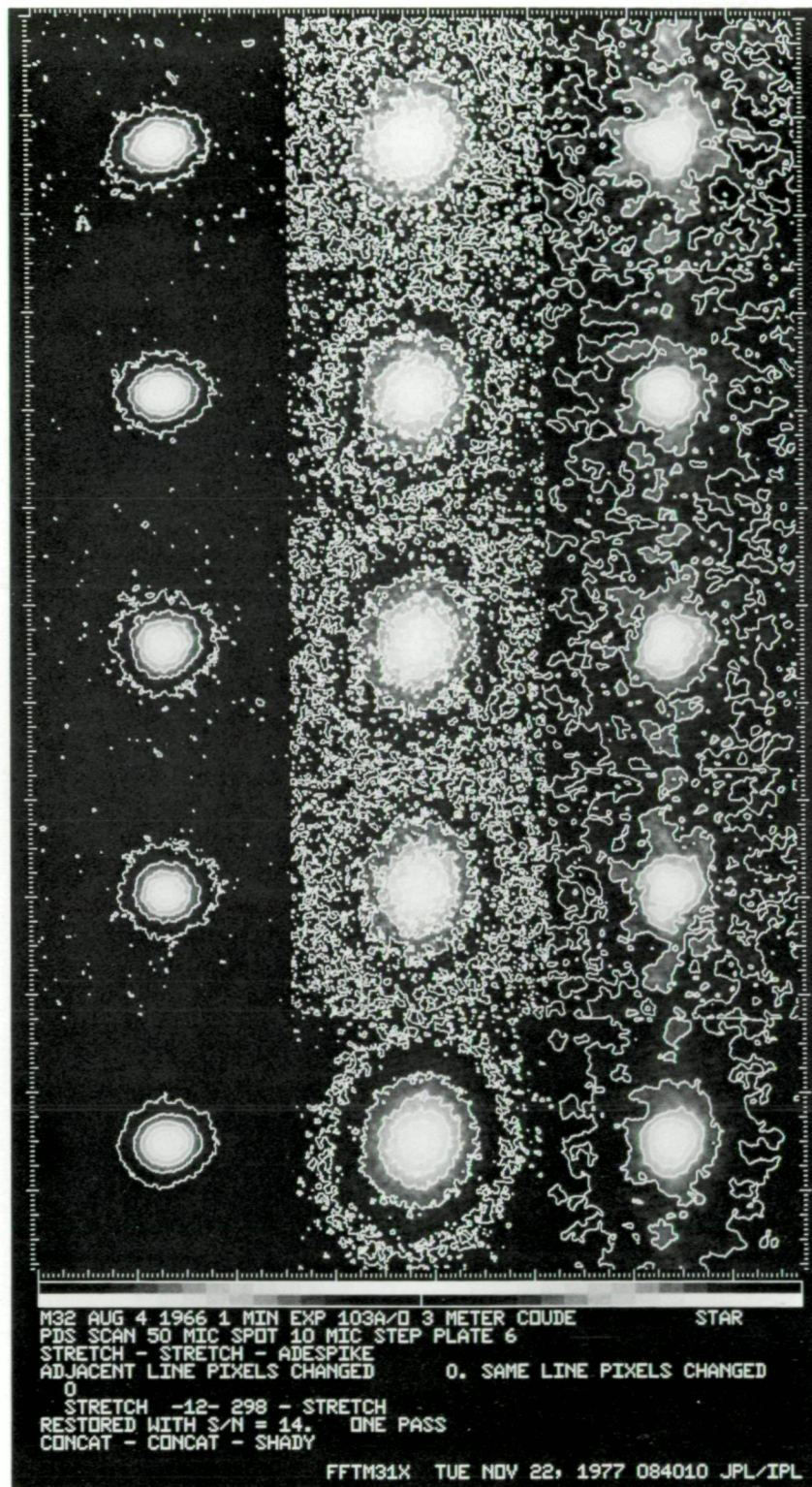


Fig. 36. Isophote contours superimposed upon the mosaic of Figure 35 (M32)



Fig. 37. Deconvolution of two plates of M87. The left side is the original, and the right side is deconvolved to separate the bright feature into two knots (M87)

ORIGINAL PAGE IS
OF POOR QUALITY

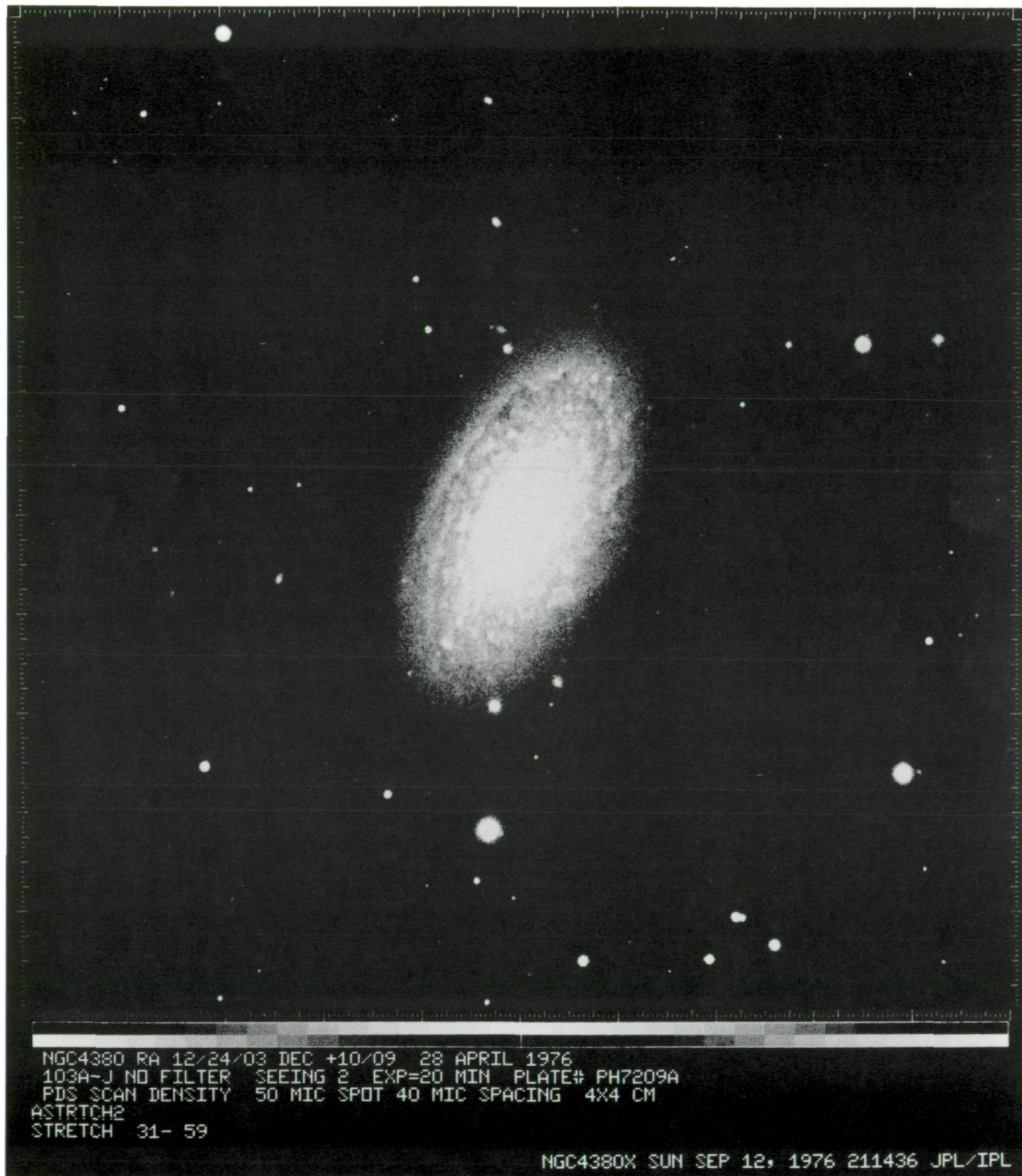


Fig. 38. Intensity image of a galaxy showing a spiral pattern which is not symmetrically textured (NGC4380)

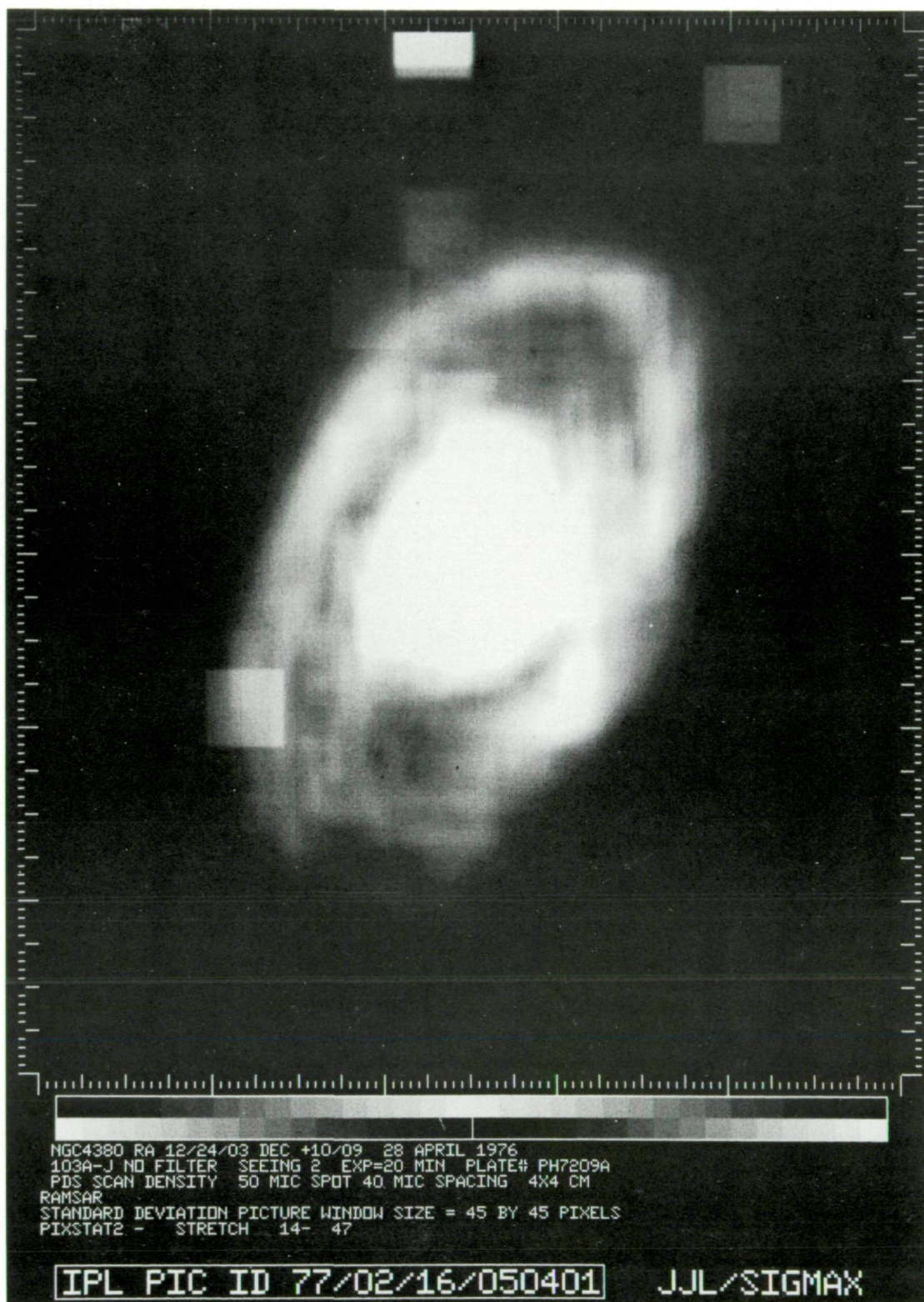


Fig. 39. A picture illustrating the local standard deviation. The break in the ring around the galaxy indicates a difference in texture between the top and bottom halves (NGC4380)

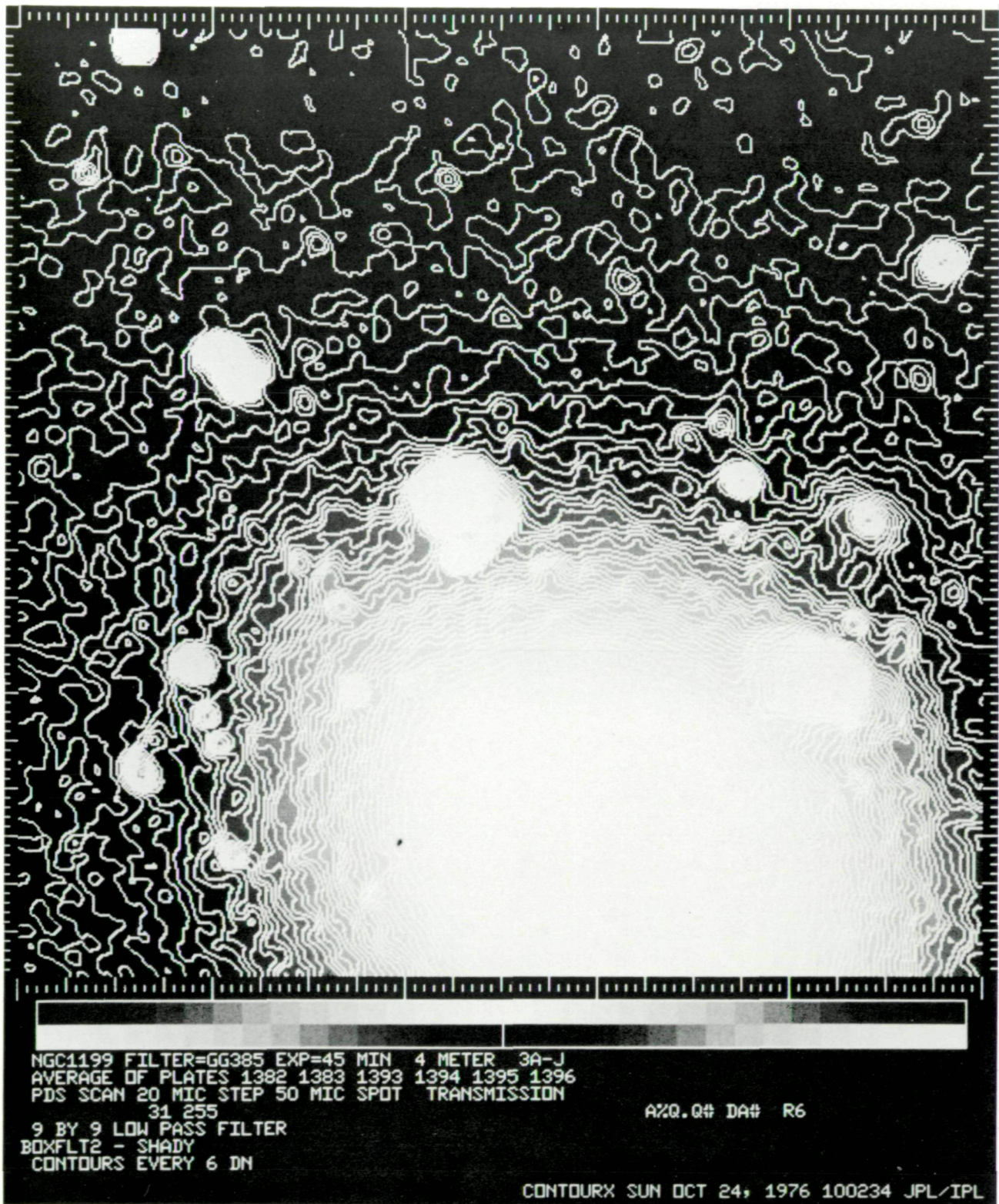


Fig. 40. Isophotes spaced at close intervals reveal the distribution of intensity in the vicinity of two line-of-sight galaxies (NGC1199)

